Engineering Fracture Mechanics 329 (2025) 111626

Contents lists available at ScienceDirect

Engineering Fracture Mechanics

journal homepage: www.elsevier.com/locate/engfracmech

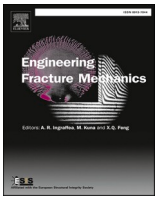

Enhancement of fracture toughness and mechanical properties of ultra-high performance concrete with ZnO nanoparticles under mixed-mode loading conditions: a multi-scale numerical investigation

Arzu Çağlar [a,*], Hakan Çağlar [b]

[a] Faculty of Engineering and Architecture, Department of Architecture, Kırşehir Ahi Evran University, Kırşehir, Turkey
[b] Faculty of Engineering and Architecture, Department of Civil Engineering, Kırşehir Ahi Evran University, Kırşehir, Turkey

ARTICLE INFO

Keywords:
Ultra-High Performance Concrete (UHPC)
ZnO Nanoparticles
Fracture Toughness
Numerical Modeling
Brazilian Disc Test
Mechanical Properties

ABSTRACT

This study is the first to thoroughly examine the effects of zinc oxide (ZnO) nanoparticles (NP) on fracture toughness, particularly in mixed-mode (I-II) conditions. It also pioneers the measurement of the impact of ZnO NP on the mechanical and fracture properties of Ultra-High Performance Concrete (UHPC). In order to simulate the behavior of ZnO nanoparticles in the UHPC matrix while taking into account different fracture modes (Mode I, Mode II, and mixed-mode I-II), the study presents a novel multi-scale finite element (FE) model. In order to improve the durability and performance of cementitious materials under complex loading scenarios, the study determines the ideal dosage of ZnO NP for increasing tensile strength and fracture toughness. The UHPC matrix behavior was simulated by the Concrete Damaged Plasticity (CDP) model, which was calibrated using experimental uniaxial compression and direct tension data. The fracture behavior of the UHPC specimens was examined using the Cracked Straight-Through Brazilian Disc (CSTBD) test configuration with different central crack inclination angles (β). The numerical model's validity was confirmed against experimental results for $\beta = 0^\circ$ and $\beta = 45^\circ$. A subsequent parametric study assessed the impact of ZnO NPs volume fraction and crack inclination angle on Mode I, Mode II, and mixed-mode (I-II) fracture toughness. Findings indicate that an optimal 0.4 wt% ZnO NPs addition significantly enhances mixed-mode fracture toughness, particularly at critical inclination angles dominated by combined tensile-shear mechanisms. While the optimal dosage for maximizing compressive strength was 0.6 wt% (yielding a 20.6 % increase), 0.4 wt% ZnO proved optimal for enhancing tensile strength (up to 40 % increase) and fracture toughness. Notably, at 0.4 wt%, the pure shear (Mode II) fracture toughness increased by over 2.1 times. This research highlights the substantial potential of ZnO NPs to improve UHPC mechanical properties and fracture resistance under complex, mixed-mode loading conditions.

1. Introduction

In recent years, the development of novel high-performance construction materials has garnered significant attention from

* Corresponding author.
E-mail address: arzu.caglar@ahievran.edu.tr (A. Çağlar).

https://doi.org/10.1016/j.engfracmech.2025.111626
Received 12 June 2025; Received in revised form 7 September 2025; Accepted 8 October 2025
Available online 10 October 2025

Nomenclature

Abbreviation

ASTM	American Society for Testing and Materials
CDP	Concrete Damaged Plasticity
CSTBD	Cracked Straight-Through Brazilian Disc
FE	Finite Element
ITZ	Interfacial Transition Zone
K_{eff}	Effective Mixed-Mode Fracture Toughness
K_{IIC}	Mode II Fracture Toughness
K_{IC}	Mode I Fracture Toughness
LEFM	Linear Elastic Fracture Mechanics
NPs	Nanoparticles
PP	Polypropylene
SEM	Scanning Electron Microscope
SF	Silica Fume
SIF	Stress Intensity Factor
SP	Superplasticizer
UHPC	Ultra-High Performance Concrete
UTM	Universal Testing Machine
w/b	Water-to-binder ratio
ZnO	Zinc Oxide

Symbols and Notation

a	Half crack length in CSTBD specimen (mm)
B	Specimen thickness (mm)
D	Diameter of CSTBD specimen (mm)
E	Elastic modulus (MPa)
f_{b0}/f_{c0}	Ratio of biaxial to uniaxial compressive strength
f_c	Uniaxial compressive strength (MPa)
f_t	Uniaxial tensile strength (MPa)
$f_I(\beta)$	Mode I geometric correction factor
$f_{II}(\beta)$	Mode II geometric correction factor
K_c	Shape factor for deviatoric stress in CDP model
K_{IC}	Mode I fracture toughness (MPa·$\sqrt{m}$)
K_{IIC}	Mode II fracture toughness (MPa·$\sqrt{m}$)
K_{eff}	Effective mixed-mode (I-II) fracture toughness (MPa·$\sqrt{m}$)
P_{max}	Peak load during CSTBD test (kN)
R	Radius of CSTBD specimen (mm)
ν	Poisson's ratio
ψ	Dilation angle in CDP model (degrees)
ϵ	Flow potential eccentricity (dimensionless)
β	Crack inclination angle relative to loading axis (degrees)

researchers worldwide [1–3]. This focus stems from the pressing need to address the escalating demands within the civil engineering sector concerning enhanced durability, superior strength, and improved structural stability of infrastructure [4,5]. Within this landscape of advanced materials, UHPC stands out as one of the most promising and advanced generations of concrete [6–8]. Its distinction lies primarily in its exceptionally high compressive strength, remarkable durability, and unique pseudo-strain hardening (or ductile) behavior under tensile stresses, offering substantial resistance against crack initiation and propagation.

Nevertheless, to further push the boundaries of UHPC performance and specifically augment its mechanical and fracture properties, innovative hybrid reinforcement strategies are continuously being explored [9]. These approaches frequently involve the synergistic combination of traditional reinforcing elements like discrete fibers with emerging nanostructured additives [10]. Nanoparticles have emerged as highly effective reinforcements in advanced materials, enabling significant improvements in mechanical properties and facilitating innovative applications across various fields of engineering and technology [11,12]. Among these contemporary strategies, the incorporation of metal oxide nanoparticles, such as Zinc Oxide (ZnO) nanoparticles (NPs), in conjunction with polymer fibers, has been proposed as a novel pathway [13–15]. This method aims explicitly to improve the material's fracture resistance and tailor its mechanical response under various failure modes. Despite this potential, comprehensive and simultaneous investigations into the combined effects of such hybrid reinforcement systems on UHPC fracture behavior, particularly through integrated numerical modeling and experimental validation, remain notably limited in the existing literature.

UHPC has garnered significant attention in civil engineering due to its superior mechanical properties and durability, making the study of its fracture toughness crucial for ensuring structural integrity [16]. Recent research within the last three years has focused on enhancing UHPC fracture characteristics through various methods, including hybrid fiber reinforcement [17], modification with amorphous alloy fibers [18], and the incorporation of recycled materials for sustainable solutions [19,20]. Studies also explore the impact of curing conditions and shrinkage-mitigating additives on UHPC fracture behavior [21], as well as its performance under extreme conditions such as low temperatures [22] and dynamic loading [23]. These advancements aim to optimize UHPC composition and processing for improved fracture resistance and broader application in construction. Researchers have explored the use of hybrid fibers to improve the fracture behavior of UHPC [24]. For instance, combining steel fibers with non-metallic fibers can synergistically enhance crack resistance. Shuo et al. [25] studied the effects of different hybrid ratios of steel fibers and plastic steel fibers, demonstrating improvements in tensile strength and fracture mode under dynamic loading. The Brazilian disc test involves diametrically compressing a circular disc specimen [26]. In the CSTBD variant, a straight notch or crack is introduced through the center of the disc along the loading diameter. This pre-existing crack helps to control the location and direction of crack propagation during the test [27]. The CSTBD configuration is particularly useful for investigating mixed-mode fracture, where both Mode I (opening) and Mode II (sliding) fracture modes are present [28]. Other variations of the Brazilian disc test include the centrally cracked Brazilian disc [29], the cracked chevron notched Brazilian disc [30], and the double-edge cracked Brazilian disk [31]. Recent studies have also investigated the role of fiber reinforcement in enhancing the fracture resistance of cementitious composites. For instance, Shi et al. [32] evaluated the fracture toughness of cement mortars reinforced with recycled carbon fibers and conducted a parallel environmental impact assessment. Zhang et al. [7] highlighted how microstructural defects such as corrosion pits accelerate crack growth in steel wires. Together, these studies emphasize the critical role of microstructural control—whether fiber bridging or nanoparticle dispersion—in governing fracture resistance.

Recent advances in the experimental characterization and numerical modeling of cementitious and composite materials have significantly enhanced the understanding of their mechanical performance and failure mechanisms [33]. Studies have employed machine learning for crack evaluation in structural components [34], developed thermal history-based prediction methods for additively manufactured alloys [35], and investigated the deformation and damage of structural elements under complex loading [36]. The influence of grout performance in challenging environments [37] and active support strategies in mining and tunneling [38] have also been explored. Furthermore, Gao et al. [39] provided insight into the constitutive behavior of fiber-reinforced concrete, underscoring the importance of advanced modeling for predicting tensile properties in engineered cementitious systems. These developments underpin the necessity for robust experimental and multi-scale modeling approaches—such as those adopted in the present study—to accurately assess and optimize the mechanical and fracture behavior of nano-engineered concrete composites. Notwithstanding the advancements achieved in the domain of fiber-reinforced UHPC production, a precise elucidation of the mechanisms by which NPs influence the fracture process, and the nature of their interaction with the concrete microstructure, persists as a significant scientific challenge. This challenge is particularly pronounced when NPs are utilized concurrently with polymeric fibers (such as the previously mentioned polypropylene (PP) fibers). In such hybrid systems, multi-scale phenomena – encompassing stress transfer across interfacial regions, potential densification of the Interfacial Transition Zone (ITZ), and the complex stress distribution fields surrounding crack tips – necessitate meticulous investigation through a combined approach integrating mechanical experimentation and sophisticated numerical modeling.

In recent years, owing to the inherent complexities and substantial costs associated with extensive experimental campaigns, finite element and theoretical techniques have emerged as a pragmatic alternative for predicting the fracture toughness of composite materials [40–42]. The significance of these techniques has amplified with advancements in computational technology and numerical solution methodologies [43,44]. Nevertheless, accurately representing the true dimensions of constituent particulates (such as aggregates and fibers) and their aspect ratios (length-to-diameter) poses inherent challenges for conventional finite element analysis across both macroscopic and microscopic modeling scales [45]. An alternative paradigm for predicting the mechanical properties of composite materials has materialized alongside the evolution of finite element methods: the direct modeling of composites at the microstructural level. Within this methodology, the constituent phases – namely the matrix (or background phase) and the reinforcing inclusions (particles or fibers) – are explicitly represented and simulated as distinct entities. By defining the interactions between these components, a more physically representative model of the composite material can be constructed. Assigning distinct material properties to each constituent allows for the evaluation of the overall mechanical response of the assemblage. For instance, Khani et al. [46] investigated the elastic properties of composites reinforced with helical and filamentous carbon nanotubes utilizing FE analysis. Pashaki et al. [47] explored the behavior of CNT-reinforced nanocomposites employing micro-FE techniques. Their research involved studying the mechanical response of such composites via two-dimensional simulations, explicitly accounting for the interaction between the NPs and the surrounding matrix. Esmaeili et al. [48] examined the influence of fiber geometrical characteristics on the tensile strain-hardening behavior of concrete through a dedicated methodological investigation. Furthermore, Esmaeili et al. [49] characterized the tensile properties of fiber-reinforced concrete employing a multi-scale Finite Element (FE) approach. In one of the pertinent recent investigations, Deng et al. [50] studied both the tensile and compressive behavior of fiber-reinforced concrete using a multi-scale FE model. Their study specifically included an examination of the influence exerted by spring- and hook-shaped fibers on the concrete's overall mechanical properties.

Despite considerable progress in research concerning the fracture behavior of UHPC, the preponderance of prior investigations has primarily concentrated on characterizing fracture responses under tensile (Mode I) and compressive loading regimes. However, less emphasis has been placed on the meticulous examination of fracture behavior under shear (Mode II) and mixed-mode (Mode I-II) conditions, particularly within the context of UHPC reinforced with PP fibers. Furthermore, although the incorporation of ZnO NPs as an additive in cementitious composites is known to significantly enhance various physical and mechanical properties, its specific

impact on the fracture behavior and toughness of UHPC, especially across different failure modes, has not yet been comprehensively and systematically investigated. Consequently, the precise role of ZnO NPs in augmenting the toughness and modifying the fracture characteristics of PP fiber-reinforced UHPC remains largely unexplored. These identified gaps in the current body of knowledge underscore the necessity for a detailed and systematic study in this area.

The principal objective of the present research is therefore to address these lacunae by developing and presenting a comprehensive framework capable of evaluating the influence of ZnO NPs on the fracture behavior of PP fiber-reinforced UHPC under diverse loading scenarios, encompassing pure tensile (Mode I), pure shear (Mode II), and mixed-mode (Mode I-II) conditions. Employing a multi-scale FE modeling approach, complemented by experimental validation, this study endeavors to expand the fundamental understanding of how ZnO NPs affect the overall mechanical characteristics and, more specifically, the fracture toughness of UHPC. Such insights are anticipated to contribute significantly to the development of more resilient and durable concrete materials for advanced applications in the construction industry.

2. Experimental program

2.1. Materials and mix proportions

In the present investigation, the primary cementitious material employed was Portland cement Type I. Supplementary cementitious materials included Silica Fume (SF), possessing a specific surface area of 18.5 m^2/g, and ZnO NPs. These NPs, characterized by a purity of 99.5 % and an average particle size of 40 ± 5 nm, were incorporated at varying dosages of 0, 0.2, 0.4, 0.6, and 0.8 wt% (wt.%) as a partial volumetric replacement for cement. The ZnO NPs were procured from US Research Nanomaterials, Inc. Further details pertaining to the characteristics of the ZnO NPs can be found in Ref. [51]. The pertinent physical and chemical properties of the Portland cement and SF utilized are presented in Table 1, while the specifications of the ZnO NPs are summarized in Table 2. Representative Scanning Electron Microscopy (SEM) micrographs of the ZnO NPs are depicted in Fig. 1, illustrating their generally spherical morphology. The SEM micrographs of the ZnO nanoparticles and PP microfibers were obtained using a TESCAN MIRA3 field emission scanning electron microscope (FE-SEM) operated at an accelerating voltage of 15 kV. Additionally, PP microfibers, conforming to the specifications detailed in Table 3 and visually represented in the SEM image in Fig. 1, were incorporated into the mixtures. A constant water-to-binder ratio (w/b) of 0.22 was maintained across all mixtures to facilitate dense particle packing. In alignment with recommendations by Paillère [52], coarse aggregates were deliberately excluded from the mix designs. Quartz sand, with a particle size distribution ranging from 0.1 mm to 0.8 mm, served as the fine aggregate. A polycarboxylic acid-based Superplasticizer (SP), characterized by a solid content between 28.5 and 31.5 wt% and a density of 1.087 g/cm^3, was employed as a high-range water-reducing admixture.

Ultrasonic waves (ultrasonication) are frequently employed to subject the NPs to high shear stresses, thereby facilitating the breakdown of these agglomerates and resulting in smaller, well-dispersed particles. This dispersion technique introduces minimal contamination, as direct contact between the dispersed particles and the ultrasonic probe is not required. Agglomeration significantly impairs the performance and reduces the efficacy of NPs; consequently, ultrasonication was utilized in this research to ensure the application of ZnO NPs with reduced agglomeration, thereby maximizing their potential beneficial effects within the composite matrix.

The mix proportions for the ZnO NP-reinforced UHPC are detailed in Table 4. The mixing procedure involved several distinct steps. Initially, to mitigate potential agglomeration and achieve a uniform dispersion of the fine particulate components, all powders (cement and SF) and the quartz sand were dry-mixed at a low speed for 5 min. Direct addition of dry ZnO NPs was deemed impractical due to their very low density, which tended to cause airborne dispersion. Therefore, the ZnO NPs were first dispersed in the mixing water using the aforementioned ultrasonication process. This aqueous suspension of ZnO NPs was then combined with the SP. Subsequently, this liquid phase (water + ZnO NPs + SP) was gradually introduced into the dry powder-sand mixture while mixing continued. After approximately 5 min of wet mixing, a fluid and homogeneous mixture was obtained. Finally, the PP fibers were added to the fresh UHPC matrix, and the entire composite was subjected to an additional 2 min of mechanical mixing to ensure adequate fiber distribution.

Table 1
Chemical properties of Cement and Silica Fume.

Property	Cement	Silica Fume
SiO_2 (Silicon Dioxide)	23 %	88 %
Al_2O_3 (Alumina)	3.50 %	2.30 %
Fe_2O_3 (Iron Oxide)	2.10 %	1.20 %
CaO (Calcium Oxide)	65 %	0.80 %
MgO (Magnesium Oxide)	2.40 %	0.60 %
SO_3 (Sulfur Oxide)	3 %	1.80 %
Na_2O (Sodium Oxide)	0.50 %	0.90 %
K_2O (Potassium Oxide)	0.10 %	2.20 %
H_2O (Water)	0.30 %	0.60 %
LOI (Loss on Ignition)	1 %	1.30 %

Table 2
Properties of ZnO NPs.

Formula	Specific surface area (m^2/g)	Purity	Diameter (nm)	Density (g/cm^3)	Morphology	Color
ZnO	40 ± 5	>99.5 (%)	40 ± 5	5.6	Spherical	White

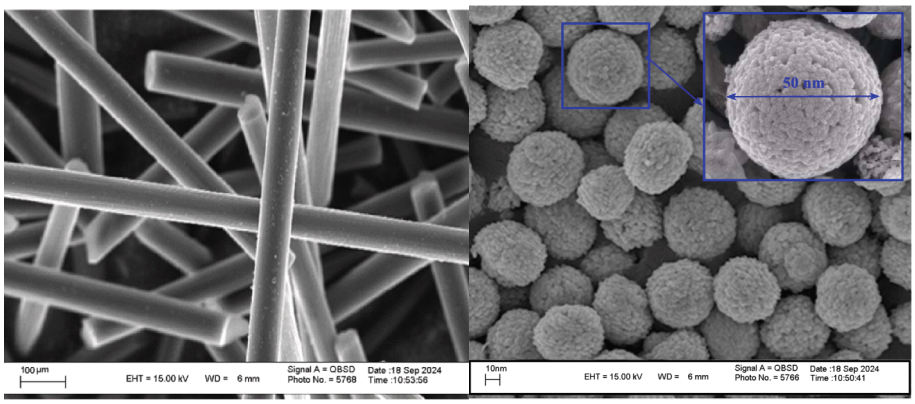

(a) (b)

Fig. 1. SEM image of (a) PP fibers, and (b) ZnO NPs.

Table 3
Mechanical properties of PP fibers.

Parameter	Value
Fiber diameter	30 ± 5 µ m
Fiber length	15 ± 2 m m
Tensile strength	550 ± 20 MPa
Tensile modulus	40 GPa
Elongation at break	1.3 %
Specific density	1150 kg/m^3

Table 4
Mix proportions of ZnO NP-reinforced UHPC.

Material	Relative weight ratio to cement
Cement	1.00
Silica fume (SF)	0.15
Quartz Powder	0.35
Superplasticizers (SP)	0.02
w/b	0.22
PP fiber	0.005
Nano-ZnO	0.0, 0.2, 0.4, 0.6, 0.8 wt%

2.2. Specimen preparation

Fresh UHPC mixtures were cast into specific molds for subsequent mechanical characterization. Cubic molds with internal dimensions of 50 × 50 × 50 mm^3 were utilized for preparing specimens designated for compressive strength testing. Concurrently, briquette-type molds, featuring a central cross-sectional area of 25 × 25 mm^2, were employed for fabricating specimens intended for direct tension testing. During the casting process, all molds were placed on a vibrating table to facilitate the removal of entrapped air and ensure adequate consolidation of the fresh mixture. The specimens were subsequently demolded approximately 24 h after casting. Following demolding, they underwent a curing regime involving immersion in lime-saturated water at ambient laboratory temperature for an additional 27 days prior to testing. After the completion of the curing period, the two load-bearing end surfaces of the cubic specimens were ground flat using a surface grinder to ensure parallel and smooth surfaces suitable for uniaxial compression loading. The experimental setups for the direct tension and compressive strength tests are presented in Fig. 2a and Fig. 2b, respectively.

To investigate the fracture behavior of the prepared materials, the CSTBD test configuration was employed. For the fabrication of the CSTBD specimens, cylindrical plastic molds with an internal diameter of 100 mm and a thickness (height) of 60 mm were used. To

Fig. 2. Experimental setup for (a) direct tension test (briquette-type specimens) and (b) compressive strength test.

introduce a well-defined, pre-existing crack at the center of the Brazilian disc specimens, a thin foam insert, measuring 2 mm in thickness, 50 mm in length (representing the crack length, *2a*), and 60 mm in depth (corresponding to the full specimen thickness), was carefully positioned within the mold prior to casting the UHPC (Fig. 3).

2.3. Experimental testing procedures

Compressive strength tests were conducted in accordance with the American Society for Testing and Materials (ASTM) C109/C109M-11 standard. A hydraulic compression testing machine with a load capacity of 10 kN was utilized. A constant loading rate of 10 kN/min was applied, and the maximum applied force (peak load) was recorded. For each mix design, three replicate specimens were tested.

The experimental setup for the direct tension test is illustrated in Fig. 2a. The briquette-type specimens were mounted within steel grip jigs, following the general principles outlined in the American Association of State Highway and Transportation Officials (AASHTO) T 132 standard. A uniaxial tensile force was applied monotonically using a Universal Testing Machine (UTM). To minimize potential eccentric loading effects, a combination of pinned and fixed support conditions was implemented within the gripping mechanism. The applied load was monitored and recorded via a load cell integrated with the testing machine. CSTBD tests were

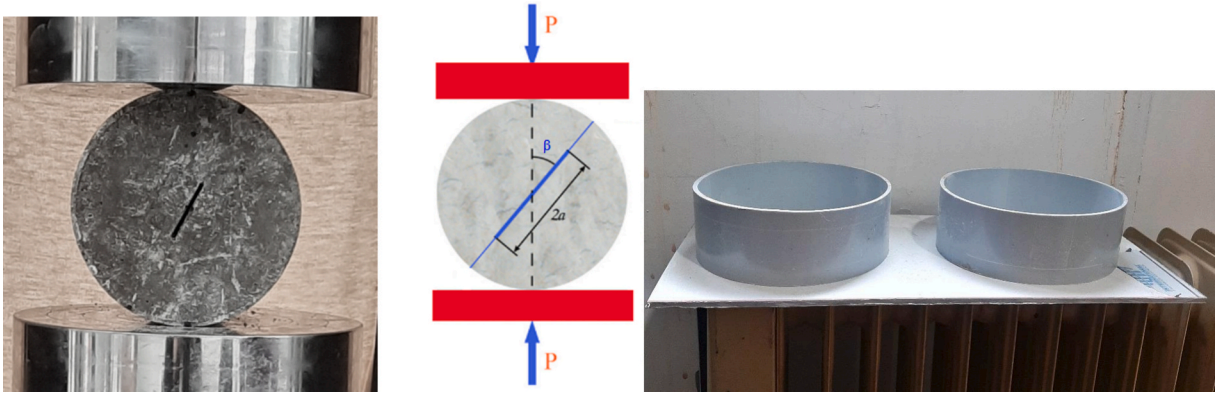

Fig. 3. CSTBD specimens utilized in the experimental tests.

performed using the aforementioned 10 kN capacity UTM. This machine is capable of applying controlled and precise loading to the concrete specimens, with digital acquisition of both the applied force and the specimen's displacement. The loading rate was displacement-controlled, maintained at a constant rate of 2 mm/min. The acquired data were utilized for plotting load–displacement curves and subsequent analysis of the UHPC's fracture behavior. The UTM automatically controlled the loading process and recorded the data with high precision. Fig. 4 shows the CSTBD specimen setup within the UTM.

The CSTBD fixture was made of electroplated steel with a thickness of approximately 100 mm, ensuring a sufficiently rigid loading frame. Specimen centering was verified by first photographing the specimen placement and then processing the images to assess the exact positioning, which achieved a centering accuracy within ±0.1 mm. The applied load was recorded by a calibrated load cell with a data acquisition frequency of 100 Hz, providing sufficient temporal resolution for monitoring crack initiation and growth.

In the CSTBD tests, the crack inclination angle (β) relative to the loading direction was set to 0° to induce predominantly Mode I fracture, 29° and 45° to achieve mixed-mode I-II fracture. These experimental tests were conducted for these three distinct loading configurations. Table 5 provides the specifications of the specimens subjected to the CSTBD tests. In Table 5, the ZnO0.0-β0 sample represents the control/reference specimen without ZnO nanoparticles, tested under Mode I (pure tension) conditions.

To evaluate the fracture toughness of UHPC specimens under different failure modes (Mode I, Mode II, and mixed Mode I–II), the CSTBD configuration was employed. In this method, the semi-circular specimens with a pre-crack of length a, inclined at an angle β with respect to the loading direction, were subjected to three-point bending. The fracture toughness values were calculated using the following relations [53]:

$$K_{IC} = \frac{P_{\max}\sqrt{\pi a}}{\pi BR} \cdot f_I(\alpha) \tag{1}$$

$$K_{IIC} = \frac{P_{\max}\sqrt{\pi a}}{\pi BR} \cdot f_{II}(\alpha) \tag{2}$$

where P_{max} is the peak load, B and R are the specimen thickness and radius respectively, and $f_I(\beta)$, $f_{II}(\beta)$ are geometry-dependent correction factors obtained via finite element simulation. The effective fracture toughness in the mixed-mode regime was then

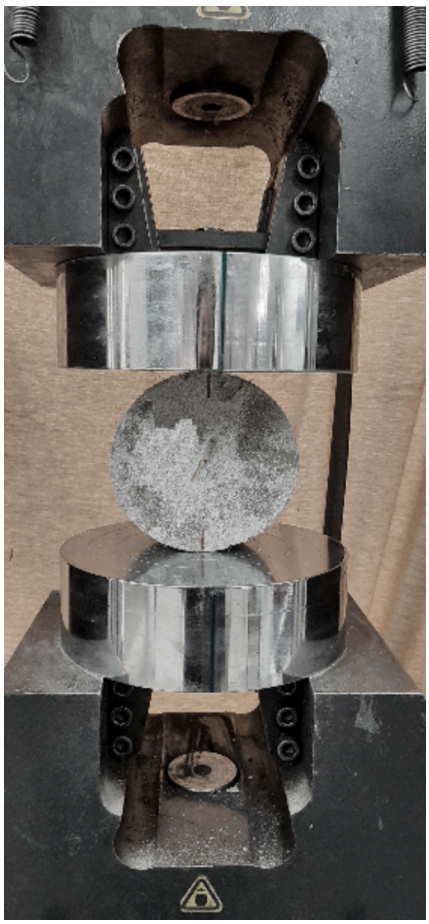

Fig. 4. Experimental setup for CSTBD fracture loading.

Table 5
Specifications of the experimental CSTBD specimens.

Sample Name	ZnO NPs Content (wt.%)	Crack Angle	Failure Mode
ZnO0.0-β0	0.0	0°	Mode I (Pure Tension)
ZnO0.2-β29	0.2	29°	Mode I-II (mixed-mode)
ZnO0.2-β45	0.2	45°	Mode I-II (mixed-mode)

calculated using [53,54]:

$$K_{\text{eff}} = \sqrt{K_{IC}^2 + K_{IIC}^2} \tag{3}$$

These equations allow for the quantification of fracture resistance under varying crack orientations. The correction functions $f_I(\beta)$ and $f_{II}(\beta)$ are the dimensionless weight function of mode-I and −II fracture toughness, respectively, considering the actual geometry and material heterogeneity of UHPC reinforced with ZnO NPs.

3. Multi-scale finite element modeling

In this research, a multi-scale FE model was employed to simulate the behavior of ZnO NP-reinforced UHPC specimens. This model is composed of three distinct, homogeneous constituent phases: the PP fiber-reinforced UHPC matrix, the ZnO NPs, and the Interfacial Transition Zone (ITZ) situated between the NPs and the UHPC matrix, as illustrated in Fig. 5. The CSTBD specimen was modeled geometrically as a cylinder with a diameter of 100 mm and a thickness of 60 mm. A pre-existing crack, characterized by a length of $2a$ and an inclination angle β relative to the vertical loading axis, was explicitly incorporated into the model geometry. Consistent with the experimental setup, the initial crack was represented with an aperture (thickness) of 2 mm and extended through the entire specimen depth (60 mm).

In this study, an innovative approach was adopted for the explicit simulation of the discrete ZnO NP phase, aiming to more accurately represent their spherical morphology. Within this framework, the ZnO NPs were modeled as discrete spherical particles with a diameter specified as 40 ± 5 nm. To achieve a statistically random distribution of these NPs within the volume of the CSTBD specimen, while adhering to the prescribed volume fractions, the Monte Carlo simulation technique was employed. This stochastic particle placement process was implemented using a custom script developed within the commercial FE software package, ABAQUS (Dassault Systèmes Simulia Corp.). The scripting procedure ensured that the ZnO NPs were randomly dispersed throughout the matrix volume and, importantly, that no geometrical overlap occurred between adjacent NPs. Fig. 6 visually depicts the resulting distribution of ZnO NPs within the CSTBD model for various volume fractions considered in the study. This method of generating a random dispersion of ZnO NPs closely mimics the anticipated distribution in actual fabricated specimens, thereby enhancing the physical realism and predictive accuracy of the subsequent FE simulations. In this study, the contribution of PP microfibers was not modeled explicitly in the finite element simulations. Instead, a constant fiber dosage (0.5 wt%) was incorporated in all mixtures, and its effect on the mechanical behavior of UHPC was captured experimentally through uniaxial compression and direct-tension tests. The measured stress–strain responses were then used to calibrate the Concrete Damaged Plasticity (CDP) parameters of the UHPC matrix. In this way,

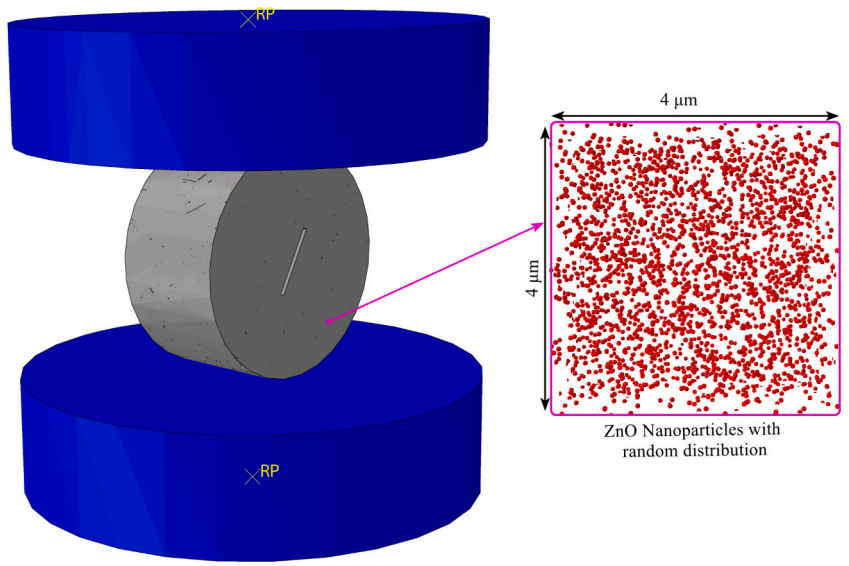

Fig. 5. Multi-scale FE model of the PP fiber-reinforced CSTBD specimen, illustrating the random distribution of ZnO NPs.

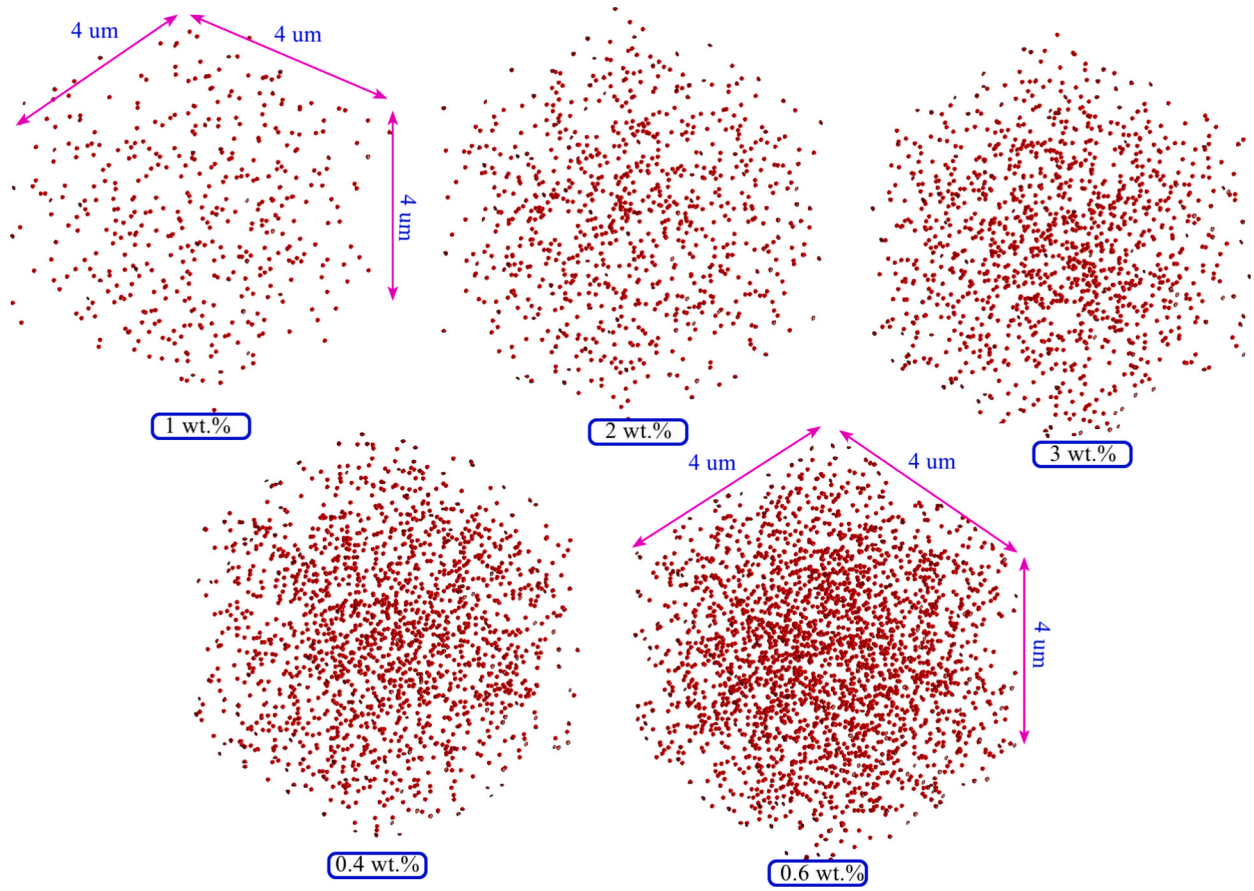

Fig. 6. Three-dimensional view illustrating the distribution of ZnO NPs within the CSTBD specimen for different ZnO NP volume fractions.

the reinforcing role of PP fibers is already embedded in the constitutive response of the matrix. The developed multi-scale FE model was therefore dedicated to explicitly representing only the ZnO nanoparticle phase and its surrounding interfacial transition zone (ITZ), using a random dispersion algorithm to simulate their stochastic distribution in the matrix. This modeling approach ensures that the numerical framework specifically isolates and evaluates the influence of ZnO nanoparticles on the fracture behavior of UHPC.

The bottom platen was completely constrained in all degrees of freedom, which corresponded to a fixed boundary condition in the FE model. According to the experimental setup, a displacement-controlled loading protocol was applied to the top platen, maintaining a constant displacement rate of 2 mm/min. A trustworthy comparison of the numerical and experimental fracture responses of the UHPC specimens is made possible by this configuration, which guarantees that the applied loading precisely replicates the experimental conditions. While the bottom platen stayed stationary throughout the analysis, the top surface of the specimen was subjected to displacement-controlled loading in order to replicate uniform compressive loading. For meshing the geometric model, three-dimensional, 20-node quadratic brick elements with reduced integration (element type C3D20R in ABAQUS) were employed. This element type is well-suited for modeling complex geometries while maintaining computational efficiency. To ensure the accuracy and convergence of the numerical results, a mesh sensitivity analysis (mesh independence study) was conducted. Based on this study, an optimal element size of 0.2 mm was selected for meshing the UHPC matrix, while a finer mesh size of 0.1 nm was utilized for discretizing the ZnO NPs themselves. This refined meshing strategy, particularly in the vicinity of potential crack paths and around the NPs, facilitates a more accurate analysis of crack initiation, propagation, and eventual failure.

Furthermore, to account for potential large deformations and material nonlinearities inherent in the fracture process, a nonlinear static analysis was performed. This type of analysis enables the accurate simulation of the material's stress–strain response under the applied compressive loading and captures the evolution of damage and crack progression. The analysis focused on investigating the stress–strain behavior of the composite material and evaluating its fracture toughness under the various imposed loading conditions (corresponding to different crack inclination angles).

In this study, the ZnO NPs were modeled using a linear elastic constitutive law. This simplification is justified by the significantly higher elastic modulus of ZnO compared to the UHPC matrix, implying that under the anticipated loading conditions, the deformation of the NPs remains within the elastic regime. The elastic modulus adopted for the ZnO NPs was 154 GPa.

To define the mechanical behavior of the UHPC matrix, the Concrete Damaged Plasticity (CDP) model, as proposed by Hafezolghorani et al. [55], was utilized. This constitutive model integrates principles of fracture energy-based damage and stiffness

degradation within the framework of continuum damage mechanics. The CDP model accounts for material deterioration resulting from both compressive crushing and tensile cracking. It employs a yield function incorporating multiple hardening/softening variables to represent the distinct damage states under tension and compression. Consequently, this model effectively captures the primary failure mechanisms observed in concrete materials.

The necessary parameters for the CDP model were primarily calibrated based on the results obtained from the experimental uniaxial compression and direct tension tests conducted on the plain UHPC specimens (i.e., those without ZnO NP addition). Supplementary parameters, where direct experimental calibration was not feasible or necessary, were adopted from relevant prior studies reported in the literature. The specific values of the CDP parameters used in this investigation are listed in Table 6.

In the finite element model, the ITZ surrounding ZnO nanoparticles was represented as a thin cohesive layer whose behavior is governed by a traction–separation law coupled with damage. The main parameters defining the ITZ response include the normal stiffness (elastic modulus ratio to matrix), Poisson's ratio, tensile strength, Mode-I fracture energy, shear cohesion, friction angle, dilation angle, and compressive fracture energy, along with the assumed ITZ thickness. These parameters control the initiation and evolution of cracking at the NP–matrix interface and thus have a significant influence on both Mode-I and mixed-mode fracture responses. Since no prior data are available for ZnO-modified UHPC, the ITZ parameters in this study were obtained through calibration against experimental CSTBD and uniaxial tension results, ensuring consistency between the numerical predictions and the measured mechanical behavior.

4. Results and discussion

This section presents an analysis of the results obtained from both the experimental program and the numerical simulations. The primary focus is to elucidate the influence of the ZnO NPs volume fraction and the initial crack inclination angle (β) on the Mode I, Mode II, and mixed-mode I-II fracture toughness of CSTBD specimens fabricated from ZnO NP-reinforced UHPC.

The discussion commences with an examination of the effect exerted by the ZnO NPs volume fraction on the fundamental mechanical properties of the UHPC, specifically its compressive and direct tensile strengths. Subsequently, the accuracy and predictive capability of the developed multi-scale FE numerical model are rigorously assessed through comparison with experimental data. Finally, a comprehensive evaluation is conducted to ascertain the impact of the investigated parameters – namely, ZnO NPs content and crack orientation – on the fracture toughness characteristics of the ZnO NP-modified UHPC.

4.1. Experimental results

4.1.1. Influence of ZnO nanoparticles on the compressive strength of UHPC

This subsection details the experimental investigation into the influence of varying dosages of ZnO NPs (0, 0.2, 0.4, 0.6, and 0.8 wt %) on the compressive strength behavior of UHPC specimens incorporating a constant 0.5 % PP fiber content. Fig. 7 illustrates the measured compressive strength of UHPC containing these different ZnO NPs contents.

As observed, the incorporation of ZnO NPs generally exerts a beneficial influence on the compressive strength enhancement of UHPC. At a ZnO NP content of 0.6 wt%, the compressive strength of the UHPC attained its peak value, representing a significant enhancement of 20.6 % relative to the reference UHPC mixture (containing 0 % ZnO NPs). Conversely, at the highest dosage investigated (0.8 wt% ZnO NPs), the rate of strength enhancement diminished, yielding the lowest observed increase of 5.4 %; nonetheless, the absolute compressive strength for this mixture remained superior to that of the reference UHPC without ZnO NPs.

These findings collectively suggest that ZnO NPs positively impact the compressive strength of UHPC. Mechanistically, upon incorporation into the UHPC matrix, the diminutive size of these NPs leads to the formation of numerous dispersion points and facilitates micro-scale interactions within the cementitious microstructure. These particles can act as micro-reinforcing agents or fillers, hindering the initiation and propagation of microcracks under applied compressive load. This observed enhancement in compressive strength is attributed to the ability of ZnO NPs to potentially absorb fracture energy and promote a more uniform distribution of internal stresses within the material structure. Consequently, the material can sustain higher stress levels before significant damage localization and macroscopic failure occur.

Table 6
Input Parameters for the concrete damaged plasticity (CDP) model for the UHPC matrix.

Parameter	Symbol	Value	Unit	Description
Elastic modulus	E	45,000	MPa	Modulus of elasticity of UHPC
Poisson ratio	ν	0.18	–	Lateral strain ratio
Tensile strength	f_t	15.2	MPa	Uniaxial tensile strength
Compressive strength	f_c	150.0	MPa	Uniaxial compressive strength
Dilation angle	ψ	36	degrees	Flow potential parameter
Flow potential eccentricity	ϵ	0.1	–	Used in Drucker-Prager function
Biaxial to uniaxial compressive strength ratio	f_{bo}/f_c	1.16	–	–
Shape factor for deviatoric stress	K_c	0.667	–	Controls yield surface shape
Viscosity parameter	μ	0.005	–	Regularization for rate-dependent effects

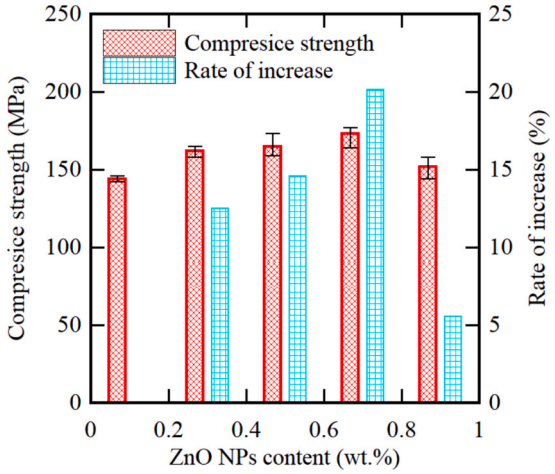

Fig. 7. Effect of ZnO NPs content on the compressive strength and the rate of compressive strength increase relative to the reference UHPC specimen.

4.1.2. Compressive behavior and toughness

The compressive stress–strain curves and the corresponding compressive toughness (calculated as the area under the stress–strain curve) for UHPC incorporating varying ZnO NPs dosages are presented in Fig. 8. It should be noted that the small nonlinear portion observed at the very beginning of the stress–strain curves originates from the partial pre-load applied during setup to secure the specimens. This minor effect is confined to a very limited strain range and does not affect the actual elastic modulus or the subsequent compressive response of UHPC. As depicted in Fig. 8(a), all specimens exhibited predominantly linear elastic behavior under relatively low initial compressive loads. As the applied load increased, the ascending portion of the stress–strain curve gradually deviated from linearity and inclined towards the strain (x) axis. This transition signifies the onset of inelastic (plastic) deformation within the ZnO NP-reinforced UHPC. It should also be noted that the small initial nonlinear region remained more pronounced in the plain UHPC specimen (0.0 wt% ZnO NP). This behavior is attributed not only to the partial preload during specimen seating, but also to the presence of microvoids and pre-existing microcracks in the matrix, which tend to close in the very early loading stage. In contrast, the incorporation of ZnO nanoparticles improves the matrix densification and reduces such microstructural imperfections, thereby minimizing this initial nonlinearity.

This observed behavior is attributed to the capacity of the ZnO NPs to potentially enhance the cohesion within the matrix and promote a more homogeneous distribution of internal stresses throughout the material structure. Acting as microscopic reinforcing elements, the ZnO NPs appear capable of absorbing a greater amount of energy during the deformation process prior to significant damage accumulation. This enhanced energy absorption capacity is reflected in the observed increase in the strain corresponding to

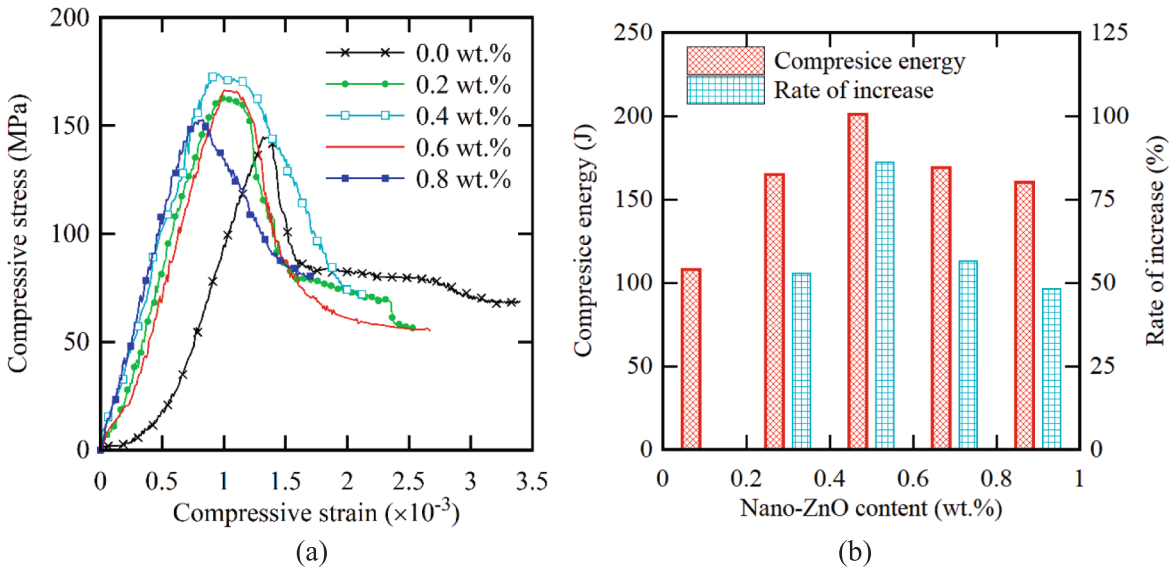

Fig. 8. (a) Compressive stress–strain curves and (b) Compressive toughness of UHPC with varying ZnO NPs contents.

the peak stress (peak strain). Furthermore, the ability of ZnO NPs to increase the peak strain suggests an improvement in the material's overall energy absorption capacity and a mitigation of the tendency towards abrupt, brittle failure under compression.

Fig. 8(b) reveals that the compressive toughness (compressive work) of the UHPC initially increases with rising ZnO NPs content, reaches a maximum, and subsequently decreases at higher dosages. This trend can be attributed to the beneficial effects of well-dispersed ZnO NPs at lower concentrations, which effectively enhance compressive toughness. In these regimes, the NPs likely impede rapid microcrack propagation and contribute to greater energy dissipation within the material structure during failure. However, at higher concentrations (e.g., 0.8 wt%), the potential for ZnO NP agglomeration within the concrete matrix increases. This can lead to stress concentrations, compromised interfacial bonding between the NPs and the matrix, and the formation of localized weak zones within the structure. These phenomena ultimately result in a reduction in the overall compressive toughness and can limit further strength improvements.

The experimental results indicate that the UHPC mixture containing 0.4 wt% ZnO NPs exhibited the most pronounced toughening effect under compression. Under these conditions, the measured compressive toughness for the UHPC with 0.4 wt% ZnO NPs was 203.5 Joules. This represents a substantial increase of 86.3 % compared to the reference UHPC specimen lacking ZnO NPs. This finding underscores the significant positive impact that an optimal dosage of ZnO NPs can have on improving both the toughness and the overall compressive response of UHPC. At this concentration, the ZnO NPs appear to be effectively dispersed within the concrete microstructure, providing enhanced energy absorption capacity during deformation without the onset of significant detrimental effects associated with particle agglomeration or weakened interfacial zones.

At supra-optimal dosages ($\geq$0.6 wt% ZnO NPs), the observed decline in strength and toughness can be attributed to agglomeration phenomena. In particular, the UHPC mixture with 0.8 wt% ZnO showed not only reduced mean compressive and tensile responses, but also noticeably larger scatter between replicates. This suggests the presence of localized weak regions associated with NP clustering and microvoids. Such agglomeration reduces the efficiency of stress transfer across the matrix–particle interface and introduces stress concentration sites that facilitate premature crack initiation.

The interpretation of performance degradation at higher ZnO dosages is further supported by literature reports on nanoparticle clustering in cementitious systems. Nayak et al. [56] demonstrated, through experimental analysis, that ZnO contents above 0.75 wt% led to an increase in average cluster size beyond 150–200 nm, coinciding with higher porosity. Wei et al. [57] similarly found that TiO_2 NPs at $\geq$0.7 wt% induced measurable increases in porosity (~10–15 %) and reduced compressive strength. Hu et al. [58] observed that ZnO NP clusters acted as stress concentrators, directly correlating with toughness degradation. These findings align with the present results, confirming that the decrease in strength and fracture toughness at 0.5–0.8 wt% ZnO is consistent with known agglomeration-induced defects in nano-modified cementitious composites.

4.1.3. Influence of ZnO nanoparticles on the tensile strength of UHPC

Fig. 9 displays the direct tensile stress–strain curves and the corresponding ultimate tensile strengths for UHPC specimens incorporating varying amounts of ZnO NPs (0, 0.2, 0.4, 0.6, and 0.8 wt%). The experimental results clearly demonstrate that the addition of ZnO NPs to UHPC exerts a significant and positive influence on both its tensile strength and, implicitly, its tensile fracture toughness. Fig. 9 shows that the first part of the compressive stress–strain curves for all samples does not follow a straight line. This happens a lot in the compressive response of UHPC and other cement-based materials. The non-linearity in the beginning is mostly because microcracks close and internal voids and pores settle down before loading. When a compressive load is put on these microstructural flaws, they start to close up, which causes the stress to rise slowly instead of in a straight line. Also, small changes in the arrangement of particles and the placement of the specimen between the platens of the testing machine can also cause this effect. When the

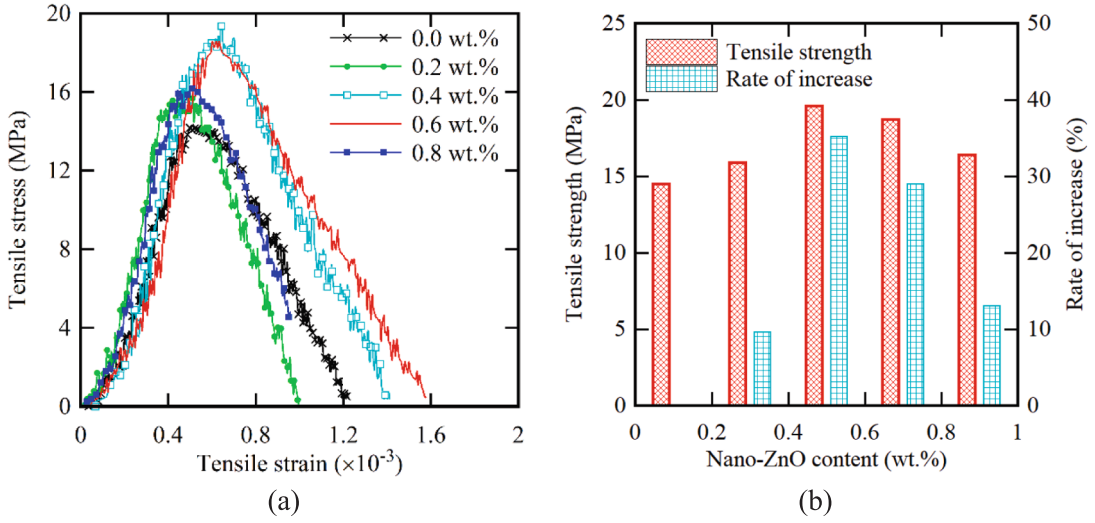

Fig. 9. (a) Direct tensile stress–strain curves and (b) Ultimate tensile strength of UHPC with varying ZnO NPs contents.

microcracks and pores are closed, the material behaves more like a linear elastic material until it gets close to the peak stress. So, this first non-linearity is a natural property of cement-based composites and doesn't mean that there was a problem with the experiment. Specifically, at a ZnO NPs content of 0.4 wt%, the tensile strength of the UHPC exhibits a substantial enhancement. The measured tensile strength increased from 14 MPa for the reference UHPC specimen (without ZnO NPs) to 19.6 MPa at this optimal dosage. This represents a considerable improvement and underscores the effectiveness of ZnO NPs in reinforcing the tensile properties of the concrete matrix. Furthermore, the rate of increase in tensile strength is notably high at this concentration, suggesting an associated improvement in the material's resistance to tensile cracking and enhanced stability under tensile loading conditions.

However, at higher ZnO NPs concentrations (specifically, 0.6 wt% and 0.8 wt%), detrimental effects become apparent. The tensile strength progressively decreases at these higher dosages, reaching approximately 16 MPa at the 0.8 wt% level. This decline is indicative of the adverse impact resulting from the agglomeration of ZnO NPs within the concrete matrix at these concentrations. Furthermore, the relative enhancement in tensile strength diminishes significantly, falling below 13 % at these dosages, indicating a reduced efficacy of the ZnO NPs in improving the tensile properties of the UHPC at these elevated concentrations.

The underlying mechanism contributing to the observed improvements (at optimal dosages) is primarily attributed to the reinforcement of the concrete's microstructure and enhanced cohesion within the matrix facilitated by the ZnO NPs. The NPs act as reinforcing agents, hindering the propagation of microcracks. Moreover, at optimal concentrations, ZnO NPs contribute to improved material stability under load. Conversely, as established, at supra-optimal concentrations, non-uniform dispersion and agglomeration lead to diminished effectiveness and overall performance degradation.

Ultimately, it can be concluded that the optimal dosage range for ZnO NPs to enhance both the tensile strength and, implicitly, the tensile toughness of the investigated UHPC lies between approximately 0.2 and 0.4 wt%. Concentrations within this range yield the most significant positive impact on tensile strength and fracture resistance, whereas dosages exceeding this optimum threshold result in the aforementioned detrimental effects. Furthermore, the enhancements observed within the optimal dosage range can be attributed to the activation of key toughening mechanisms, such as crack deflection and nano-scale bridging effects facilitated by the well-dispersed NPs. This microstructural enhancement is also corroborated by observations of the fracture surface morphology (Fig. 10), whereby the crack paths exhibit increased tortuosity, contributing to the enhanced overall fracture resistance of the material. Fig. 10 shows the ways that the UHPC specimens reinforced with ZnO NPs became tougher. These include crack bridging, where spherical nanoparticles bridge across cracks and make it harder for them to spread; particle debonding at the nanoparticle-matrix interface, which uses up energy and makes the material tougher; and overall energy dissipation by the nanoparticles, which makes the composite less brittle. These mechanisms are in line with what other researchers have found, which shows that nanoparticle debonding and crack bridging are very important for making composites stronger [59]. As illustrated in the Fig. 10a, the crack path exhibits significant tortuosity (highlighted with dashed lines), which increases the fracture surface area, impedes crack propagation, and enhances energy absorption. Conversely, Fig. 10b demonstrates smoother crack paths at higher ZnO NP dosages, resulting in lower energy dissipation and reduced fracture toughness.

4.2. Numerical results

4.2.1. Mesh independence analysis

Table 7 displays the findings of the mesh independence analysis for the ZnO0.2-β29 condition. In order to ensure accurate and dependable numerical results without incurring needless computational costs, this analysis was carried out to identify the ideal mesh size for the finite element simulations. Mesh sizes ranging from 1.0 mm to 0.1 mm were taken into consideration, and the associated

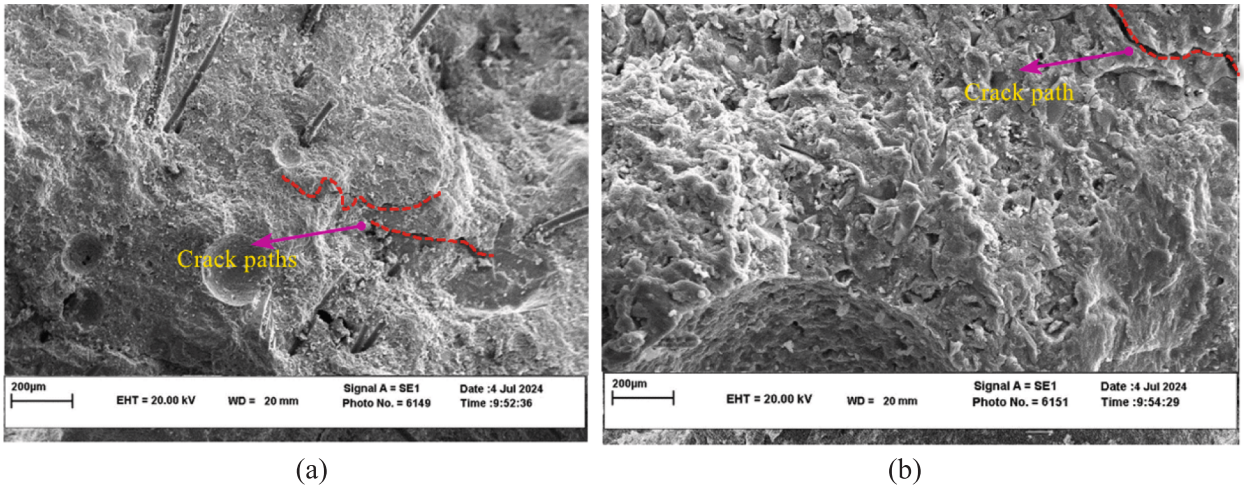

Fig. 10. SEM micrographs illustrating the fracture surface morphology of UHPC specimens with varying ZnO NPs contents, (a) 0.2 wt% and (b) 0.8 wt%.

Table 7
Mesh independence analysis results.

Mesh Size (mm)	Fracture Load (kN)	Percentage Change in Fracture Load (%)	Stress Distribution Accuracy (%)	Number of Nodes	Computational Time (Minutes)
1.0	80.5	–	98.2	250,000	12
0.5	83.2	2.63 %	99.1	450,000	20
0.2	84.3	0.76 %	99.5	900,000	40
0.1	84.5	0.09 %	99.8	1,800,000	75

computational times, number of nodes, fracture loads, and accuracy of the stress distribution were noted. Table 7 demonstrates that the fracture load predictions stabilized with mesh sizes of 0.2 mm and smaller, with the fracture load changing by only 0.76 % from the 0.2 mm mesh to the 0.1 mm mesh. As the mesh got finer, the accuracy of the stress distribution also increased, reaching 99.8 % with the 0.1 mm mesh. However, as the mesh size shrank, the computational time increased significantly; for example, the 0.1 mm mesh took 75 min to run, while the 1.0 mm mesh took 12 min.

As the mesh was refined, the number of nodes rose proportionately, demonstrating the increased computational complexity. These findings led to the selection of a mesh size of 0.2 mm as the ideal ratio of computational efficiency to accuracy, yielding dependable predictions at a reasonable computational cost. By confirming that further refinement beyond a 0.2 mm mesh does not significantly improve the accuracy of the fracture load predictions, this analysis guarantees the validity of the simulation results.

4.2.2. Determination of ITZ parameters

Because the effect of ZnO nanoparticles (NPs) on the NP–matrix interfacial transition zone (ITZ) has not been previously quantified for UHPC, the ITZ constitutive parameters were identified through an inverse calibration against the present experiments. The calibration targeted the CSTBD responses at $\beta = 0^\circ$ (Mode I) and $\beta = 45^\circ$ (mixed I–II), complemented by the uniaxial direct tension curves. The objective was to minimize the discrepancy between numerical predictions and measurements in terms of (i) initial tangent stiffness, (ii) peak load, (iii) post-peak softening slope, and (iv) crack-path tortuosity. The ITZ around each ZnO NP was modeled as a thin cohesive/damageable layer embedded between the linear-elastic ZnO particle and the CDP-governed UHPC matrix. The ITZ response in tension/shear followed a traction–separation law coupled to damage; in compression it was considered non-damaging with contact and friction. Identification procedure summarized as follows:

1. Initialization from literature bounds. Parameter bounds were chosen from micromechanical/SEM-based studies on nano-modified cementitious ITZs (typical ranges shown in the "Bounds" column of Table 8).

2. Screening & sensitivity. A Latin hypercube design sampled the bounds; sensitivity to each parameter was ranked by its effect on the four targets above.

3. Inverse optimization. A multiobjective cost J was minimized:

$$J = \sum_k \frac{\left|R_k^{\text{num}} - R_k^{\text{exp}}\right|}{R_k^{\text{exp}}} w_k \tag{4}$$

where R_k are the target response metrics and w_k their weights (equal weights used unless stated otherwise).

4 Cross-validation. The calibrated set was verified against $\beta = 29^\circ$ and $\beta = 90^\circ$ simulations without further tuning.

The calibrated ITZ exhibits (i) higher tensile/shear capacity at the optimal ZnO dosage (0.4 wt%), consistent with the observed increase in crack tortuosity and energy dissipation (Fig. 10), and (ii) a modest increase in normal stiffness relative to the plain mix. Parametric perturbations (±10 %) around the calibrated values altered the CSTBD peak load by <5 % for stiffness-like parameters but up to ~8 % for cohesive strengths/fracture energies, confirming that toughness-related ITZ parameters dominate the mixed-mode response.

4.2.3. Validation of the numerical model

To validate the predictive capability of the proposed multi-scale FE model, its simulation results were rigorously compared against the experimental data obtained from the CSTBD fracture tests conducted on various specimens (as specified in Table 5). Fig. 11

Table 8
Calibrated ITZ parameters used in the simulations.

Parameter (unit)	Symbol	Bounds used in screening	Calibrated values			
			Plain UHPC	0.2 wt% ZnO	0.4 wt% ZnO (optimal)	0.6 wt% ZnO
ITZ normal stiffness (ratio to matrix modulus)	E_{ITZ}/E_m	0.6 – 1.1	0.75	0.85	0.95	0.90
Poisson's ratio (–)	ν_{ITZ}	0.18 – 0.24	0.21	0.21	0.22	0.21
ITZ tensile strength (ratio to matrix tensile strength)	$f_{t,ITZ}/f_{t,m}$	0.5 – 1.0	0.70	0.80	0.90	0.80
Mode-I fracture energy (ratio)	$G_{f,I}^{ITZ}/G_{f,m}$	0.6 – 1.2	0.80	0.95	1.10	0.95
Shear cohesion (ratio to matrix tensile)	$c_{ITZ}/f_{t,m}$	0.6 – 1.2	0.85	0.95	1.05	0.95

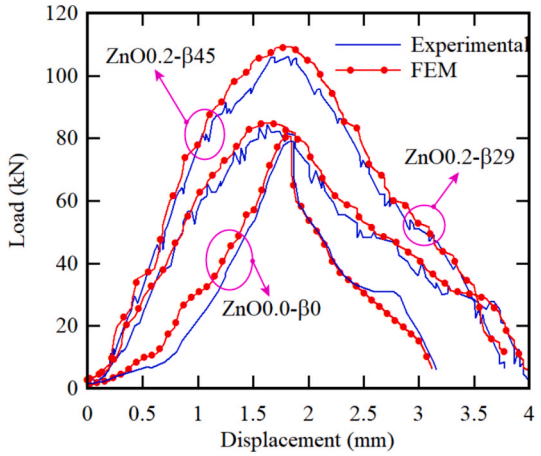

Fig. 11. Load-displacement behavior from experimental CSTBD tests compared with numerical model predictions for normal and ZnO NP-reinforced UHPC.

presents a comparison of the experimentally measured and numerically predicted load–displacement behaviors for both plain UHPC and ZnO NP-reinforced UHPC specimens under the Brazilian test configuration.

As illustrated in Fig. 11, the developed FE model demonstrates a commendable capability to accurately predict the fracture response of the CSTBD specimens. A generally good agreement is observed between the numerical predictions and the experimental curves. Nevertheless, a slightly larger, albeit still acceptable (~5%), discrepancy is noted for specimens incorporating higher NP contents. This deviation likely reflects the inherent complexities associated with the multi-scale modeling of such highly heterogeneous materials. These complexities include, but are not limited to: accurately representing the random distribution and orientation of the PP fibers within the matrix; precisely modeling the behavior of the ITZ surrounding the NPs, potentially involving complex slip and debonding mechanisms; and accounting for the inherent size dispersion of the ZnO NPs. Furthermore, a portion of this observed difference might stem from a potential physical increase in porosity within the laboratory specimens, possibly arising from the addition of minor amounts of extra water during mixing to compensate for any workability reduction caused by the NPs. Such an increase in porosity could lead to a slight reduction in the experimentally measured strength characteristics compared to the idealized numerical model.

4.2.4. Behavior of CSTBD specimens

Proceeding with the discussion, the influence of various parameters on the fracture characteristics of the CSTBD specimens is now examined based on the numerical simulation results. Fig. 12 specifically illustrates the effect of the ZnO NPs volume fraction on the predicted load–displacement response of CSTBD specimens under pure Mode I fracture conditions (crack inclination angle $\beta = 0°$), as obtained from the multi-scale FE analysis.

As depicted, the general trend indicates that increasing the ZnO NPs volume fraction up to 0.4 wt% leads to an enhancement in the

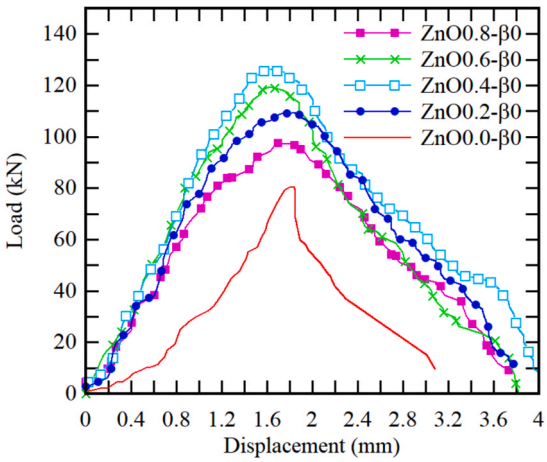

Fig. 12. Influence of ZnO content on the load–displacement curves of CSTBD specimens under Mode I ($\beta = 0°$) loading, obtained from FE simulations.

fracture load capacity of the specimens. However, further increments in ZnO content (exceeding 0.4 wt%) result in a decrease in the fracture resistance of the CSTBD specimens, a reduction clearly visible in Fig. 12 for the 0.6 wt% ZnO case.

Fig. 12 also highlights the contrasting behaviors. The plain UHPC (without NPs) exhibits minimal resistance to crack propagation and limited energy absorption capacity after reaching its peak load under the diametral compressive loading, resulting in an abrupt post-peak load drop. In contrast, the UHPC incorporating ZnO NPs demonstrates a distinct post-peak behavior characterized by a more gradual reduction in load-carrying capacity. This gradual softening response indicates enhanced energy absorption, facilitated by stress transfer mechanisms across the crack faces, notably attributed to nanoparticle bridging effects.

Based on these numerical results, the optimal utilization of 0.4 wt% ZnO NPs in UHPC significantly enhances crack control and provides increased mechanical restraint within the concrete matrix under Mode I loading. This improvement contributes to a substantial increase in the effective tensile strength or, more precisely, the Mode I fracture resistance of the CSTBD specimen under pure Mode I conditions, with enhancements reaching up to 56 % compared to the reference UHPC.

Fig. 13 illustrates the crack propagation patterns observed in representative CSTBD specimens under different fracture conditions, specifically comparing numerical predictions with experimental observations where applicable. The images show the stress

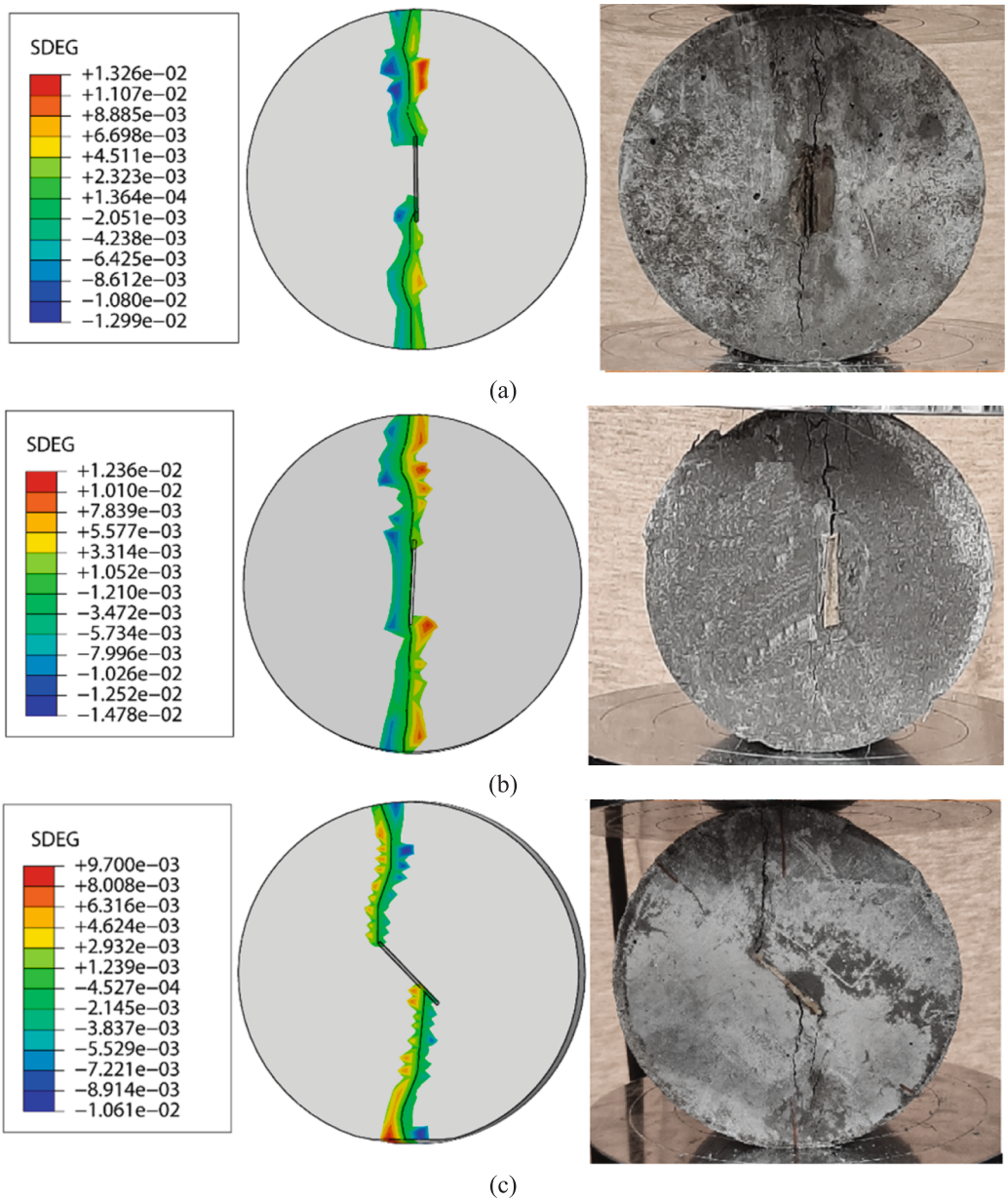

Fig. 13. Comparison of crack patterns in CSTBD specimens under different fracture modes and ZnO contents: (a) 0.0 wt% ZnO NPs, $\beta = 0^\circ$ (Mode I); (b) 0.2 wt% ZnO NPs, $\beta = 0^\circ$ (Mode I); and (c) 0.2 wt% ZnO NPs, $\beta = 45^\circ$ (Mixed Mode I-II).

deformation energy gradient (SDEG) observed during the fracture process, as simulated in ABAQUS. The SDEG is used to identify regions of significant energy dissipation and material deformation. It is evident that the multi-scale FE approach developed in this research effectively predicts the macroscopic crack propagation path within the specimens. However, it is important to acknowledge that various inherent uncertainties, such as the stochastic distribution and orientation of the PP fibers, the presence of unavoidable porosity, and the complex nature of the calcium silicate hydrate (C-S-H) gel layers forming around the PP fibers within the matrix, may lead to minor deviations in the precise trajectory of microcrack growth compared to the idealized numerical simulation.

4.2.5. *Influence of crack inclination angle on fracture load*

Fig. 14 illustrates the effect of the crack inclination angle (β) on the peak fracture load obtained from the CSTBD tests for UHPC specimens reinforced with varying amounts of ZnO NPs. The results clearly indicate that the peak load exhibits a significant dependence on the crack inclination angle. Variations in β alter the stress distribution state near the crack tip, consequently influencing the propagation path and resistance to fracture.

As the crack inclination angle transitions from $\beta = 0^\circ$ towards intermediate angles (approaching 45°-50°), a discernible decrease in the peak fracture load is observed. Subsequently, as β increases further beyond this minimum point, the peak load tends to increase again. This characteristic U-shaped trend is consistent across both the reference UHPC specimens and those modified with ZnO NPs. The addition of ZnO NPs, particularly at dosages of 0.2 wt% and 0.4 wt%, demonstrably enhances the material's cohesion and overall strength, resulting in higher peak fracture loads across the range of angles investigated compared to the reference material. Within this optimal dosage range, the ZnO NPs likely contribute to mitigating microcrack initiation and enhancing the material's toughness.

For the reference UHPC specimens (without ZnO NPs), the minimum peak fracture load is observed to occur at an inclination angle of approximately $\beta = 50^\circ$. This suggests that at this specific orientation, the combination of tensile and shear stresses near the crack tip creates a critical condition where less external load is required to initiate and propagate tensile fracture.

Conversely, with the addition of ZnO NPs, the angle at which the minimum peak fracture load occurs tends to shift towards lower values. This shift is indicative of the strengthening effect imparted by the ZnO NPs, altering the material response to combined tensile and shear stresses. Notably, for the specimens containing 0.8 wt% ZnO NPs, the minimum peak fracture load occurs at a lower angle of approximately $\beta = 43.8^\circ$. This observation suggests that ZnO NPs modify the crack propagation behavior and enhance interfacial adhesion or matrix strength, thereby altering the critical angle for minimum fracture resistance. In essence, the improved stress distribution and microstructural reinforcement provided by the ZnO NPs cause the minimum fracture load (corresponding to the most critical combination of Mode I and Mode II stresses for fracture initiation) to occur at a slightly different, generally lower, inclination angle compared to the plain material.

Consistently, the overall minimum load tends to occur at angles where the shear component (Mode II) becomes increasingly dominant, which is typically observed around or slightly above 45° in experimental CSTBD tests due to frictional effects and complex stress states. The absolute maximum peak fracture load invariably occurs under pure Mode I conditions, corresponding to $\beta = 0^\circ$. The results presented in Fig. 14 clearly demonstrate that the addition of ZnO NPs to UHPC significantly influences the peak fracture load across the spectrum of crack inclination angles investigated. For the reference specimen (0 % ZnO NPs), the maximum fracture load, occurring at $\beta = 0^\circ$ (Mode I), is approximately 77 kN. As the crack inclination angle increases, the fracture load decreases, reaching its minimum value of approximately 43.5 kN at $\beta = 50^\circ$. Beyond this angle, the fracture load increases again, attaining a value of about 56.8 kN at $\beta = 90^\circ$. This observed trend, characterized by an initial decrease followed by an increase in fracture load with increasing β, is typical for conventional concrete materials tested under CSTBD conditions.

In stark contrast, the specimens containing the optimal dosage of 0.4 wt% ZnO NPs exhibit substantially higher fracture resistance. The peak load at $\beta = 0^\circ$ for this mixture is approximately 125 kN, significantly greater than the reference case. While the load still decreases with increasing β, the minimum fracture load occurs at a slightly shifted angle of $\beta = 46.8^\circ$, and the minimum load itself is

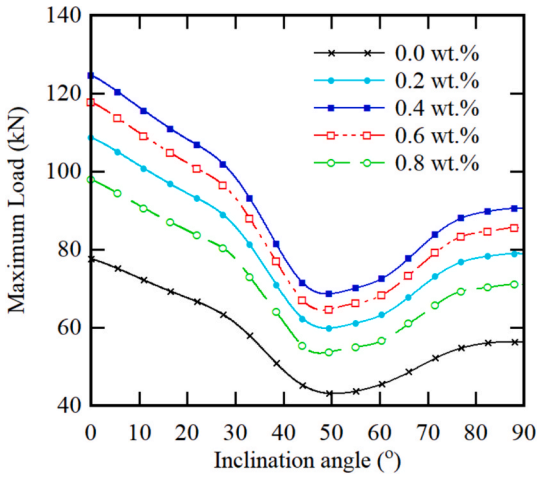

Fig. 14. Influence of crack inclination angle and ZnO NP content on the peak Brazilian fracture load.

considerably higher at 69 kN. Furthermore, the fracture load at $\beta = 90^\circ$ for the 0.4 wt% ZnO NPs specimen reaches approximately 90 kN. This represents an increase of approximately 56 % compared to the reference specimen's load of 56.8 kN at the same angle ($\beta = 90^\circ$).

This marked improvement in fracture load across various angles strongly indicates the positive contribution of ZnO NPs towards enhancing the stability and toughness of the UHPC. Consequently, the incorporation of 0.4 wt% ZnO NPs leads to a notable enhancement in the material's effective tensile strength and its overall resistance to fracture under mixed-mode conditions. This underscores the reinforcing effect of the ZnO NPs, which likely promote a more uniform internal stress distribution and improve the interfacial bond strength within the concrete matrix, thereby enhancing the material's performance under complex loading scenarios.

4.2.6. Fracture toughness analysis

The CSTBD specimens with pre-existing cracks provide a viable configuration for estimating the fracture toughness under Mode I, Mode II, and mixed-mode I-II conditions. Utilizing established theoretical relationships, specifically Eqs. (1)-(3), allows for the calculation of the stress intensity factors (and thus fracture toughness) corresponding to the peak loads obtained at various initial crack inclination angles (β) from the FE simulations.

Figs. 15–17 depict the Mode I (K_{IC}), Mode II (K_{IIC}), and potentially an equivalent mixed-mode I/II fracture toughness, as predicted by the multi-scale FE approach, plotted against the crack inclination angle for different ZnO NPs contents. A general observation across these figures is that the fracture toughness tends to increase with the addition of ZnO NPs, particularly up to the optimal dosage of 0.4 wt%.

Specifically examining Fig. 15, the Mode I fracture toughness (K_{IC}) decreases as the crack angle β increases from 0°. It reaches a value of zero at an angle of approximately $\beta = 15.6^\circ$, subsequently becoming negative and increasing in magnitude (becoming more negative) until it reaches its maximum negative value at $\beta = 90^\circ$. At an inclination angle of 15.6°, the Mode I fracture toughness K_{IC} is zero, indicating purely shear-dominated fracture behavior (Mode II). At crack inclination angles $\beta > 15.6^\circ$, negative values of K_{IC} are observed, indicating the presence of compressive normal stresses at the crack tip. The classical LEFM framework, which assumes that cracks open, may not work completely in this regime. Instead, shear under compression is probably what controls the fracture behavior. This could mean that the crack faces touch or rub against each other, which would cause stick–slip behavior. The normal SIF analysis doesn't take into account things like frictional resistance at the crack faces or the formation of shear zones, which are important for this non-opening regime. We talk about the problems with the SIF-based approach in this case and agree that more advanced models, like cohesive zone models or contact-based formulations, may be needed to accurately predict fracture in these kinds of situations. At the inclination angle of $\beta \approx 15.6^\circ$, the calculated Mode-I fracture toughness (K_{IC}) becomes zero. Physically, this corresponds to a condition where the crack experiences no effective tensile opening and is instead dominated by shear under compressive normal stresses. In this regime, the fundamental assumptions of linear elastic fracture mechanics (LEFM)—traction-free crack faces and stress intensity factors describing tensile crack opening—are no longer strictly valid. Rather, frictional contact and possible stick–slip sliding may govern the fracture process. The negative values of K_{IC} predicted at larger β therefore should not be interpreted as "negative toughness" but as an indication of compression-shear dominated fracture outside the classical LEFM domain.

Conversely, as shown in Fig. 16, the Mode II fracture toughness (K_{IIC}) initially increases at lower angles, peaks at an inclination angle of approximately $\beta = 26.8^\circ$, and then decreases thereafter. As β increases beyond 26.8°, K_{II} diminishes, eventually reaching zero at $\beta = 90^\circ$. It is noteworthy that the Mode II fracture toughness value corresponding to the angle $\beta = 15.6^\circ$ (where K_{IC} is zero) increases significantly with the addition of 0.4 wt% ZnO NPs. The calculated K_{IIC} value at this specific angle rises from 0.049 MPa$\sqrt{m}$ (for the reference UHPC) to 0.156 MPa$\sqrt{m}$. This represents a substantial enhancement factor of approximately 2.14 in the Mode II fracture toughness component at this particular inclination angle, directly attributable to the presence of the ZnO NPs.

The diagram presented in Fig. 17 illustrates the influence of both the crack inclination angle (β) and the ZnO NPs content on the effective fracture toughness (denoted as K_{eff}) under mixed-mode I-II loading conditions for the UHPC material. This plot clearly indicates that increasing the percentage of ZnO NPs (up to the optimal 0.4 wt%) leads to a substantial enhancement in the effective fracture toughness across all investigated crack inclination angles, although the behavior exhibits nonlinearity and pronounced angular dependence. Furthermore, Fig. 17 confirms that the mixed-mode fracture toughness (K_{eff}) for the UHPC incorporating ZnO NPs consistently surpasses that of the plain UHPC without NPs. Moreover, as the crack inclination angle increases (moving towards higher Mode II contributions), the beneficial effect of the ZnO NPs on enhancing K_{eff} becomes increasingly prominent. The markedly higher toughness of the ZnO NP-modified UHPC compared to its plain counterpart imparts enhanced resistance against abrupt failure. This enhanced toughness is attributed primarily to the three-dimensional dispersion of the ZnO NPs within the UHPC matrix. Consequently, when a crack initiates and propagates, these dispersed NPs can establish mechanical bridging connections across the crack faces in multiple directions, effectively impeding crack propagation and requiring greater energy for fracture. As a result, the fracture toughness of UHPC containing ZnO NPs consistently exceeds that of conventional UHPC.

Interestingly, the effective fracture toughness values for both the ZnO NP-modified and plain UHPC are approximately equivalent only within a narrow range of inclination angles, specifically between 10° and 20°. Across all specimen types investigated (from $\beta = 0^\circ$ to 90°), the overall trend of K_{eff} exhibits a distinct minimum value occurring within this 10°-20° angular range. Subsequently, as the angle increases beyond this minimum, the fracture toughness progressively increases. This characteristic behavior signifies the sensitivity of UHPC to the specific combination of tensile and shear stresses imposed by the mixed-mode loading. Angles within the 10°-20° range appear to represent the condition of greatest structural vulnerability or lowest resistance to mixed-mode fracture initiation for this material system under the CSTBD configuration. At the critical angle where the minimum K_{eff} occurs (approximately 15°), the fracture toughness for the reference specimen (without NPs) is measured to be around 0.09 MPa$\sqrt{m}$. In contrast, the corresponding value for the specimen containing 0.4 wt% ZnO NPs is approximately 0.15 MPa$\sqrt{m}$, representing a significant

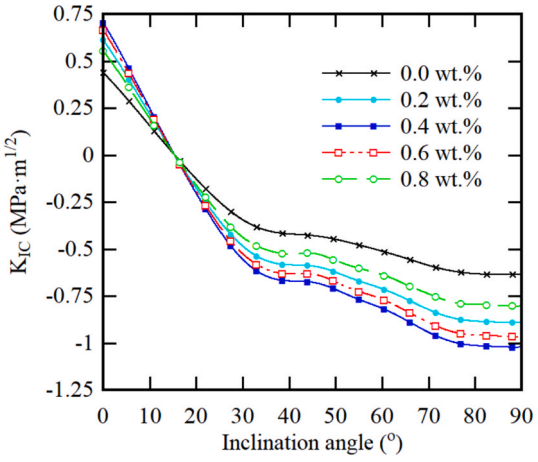

Fig. 15. Influence of crack inclination angle and ZnO NP content on the Mode I fracture toughness (K_{IC}) of ZnO NP-reinforced UHPC.

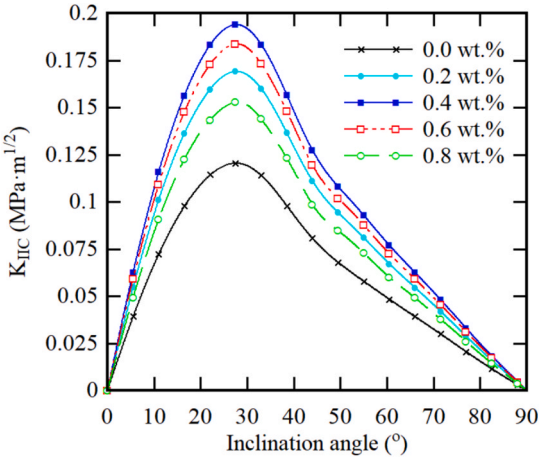

Fig. 16. Influence of crack inclination angle and ZnO NP content on the Mode II fracture toughness (K_{IIC}) of ZnO NP-reinforced UHPC.

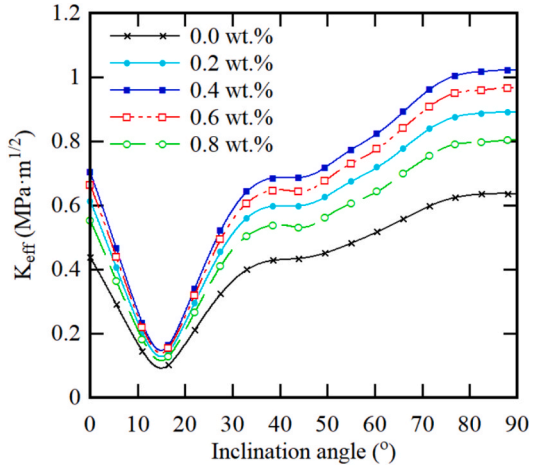

Fig. 17. Influence of crack inclination angle and ZnO NP content on the effective mixed-mode I-II fracture toughness (K_{eff}) of ZnO NP-reinforced UHPC.

improvement exceeding 67 %. Additionally, these results reaffirm the earlier finding that utilizing supra-optimal dosages of ZnO NPs (e.g., 0.6 wt% or higher) can lead to a degradation rather than an enhancement of the material's fracture properties.

4.2.7. Sensitivity and uncertainty analysis

To quantify the influence of constitutive and microstructural assumptions on the predictions, we conducted (i) a local one-at-a-time sensitivity study with ±10 % and ±20 % perturbations, and (ii) a Monte Carlo (MC) analysis over random NP placements and alternative PP fiber orientation states. The metrics examined were peak load and fracture toughness components K_I, K_{II}, and K_{eff} at $\beta = 0^\circ$, 15° (within the minimum K_{eff} range), 45°, and 90°.

Local sensitivity. At $\beta = 45^\circ$, ±10 % perturbations to ITZ cohesive strengths ($f_{t,ITZ}$) and Mode-I fracture energy ($G_{f,I,ITZ}$) changed peak load by 6–8 % and K_{eff} by 7–8 %, whereas the same perturbation to ITZ normal stiffness altered peak load by ≤ 3 % and K_{eff} by ≤ 3 %. Adjusting the CDP tensile softening slope by ±10 % yielded ~4–6 % changes in peak load and ~4–5 % in K_{eff}. Results for ±20 % followed the same ranking (Table 9).

PP fiber distribution. Transitioning from isotropic orientation to mild alignment (von-Mises–Fisher $\kappa \approx 3$) changed peak load by ≤ 3.2 % and K_{eff} by ≤ 4.1 % across β. Varying PP volume fraction by ±0.1 % (absolute) around the nominal produced ≤ 3 % variation in both metrics. These effects are within experimental scatter, supporting the homogenized-matrix treatment used in Section 3.

Monte Carlo uncertainty. For N = 50 random NP realizations (preserving the specified volume fraction) and two fiber-orientation states (isotropic/mildly aligned), the 95 % CI of peak load corresponded to CoV 3–5 % for $\beta = 0^\circ$ and 90°, and 4–7 % for $\beta = 15^\circ$–45°. The CoV of K_{eff} was 4–9 %, with the widest bands near $\beta \approx 15^\circ$. Importantly, in all realizations the 0.4 wt% ZnO case remained superior to the reference and supra-optimal dosages, preserving the main conclusions.

5. Conclusions

This study demonstrates, through a validated three-dimensional (3D) multi-scale finite element (FE) model, that optimized incorporation of Zinc Oxide (ZnO) nanoparticles (NPs) substantially enhances the mixed-mode fracture toughness of Ultra-High Performance Concrete (UHPC), providing crucial insights into its behavior under complex shear-tensile loading scenarios. The developed model explicitly represented the polypropylene (PP) fiber-reinforced UHPC matrix, randomly dispersed spherical ZnO NPs, and the NPs-matrix Interfacial Transition Zone (ITZ). Its predictive accuracy was rigorously confirmed against experimental data from Cracked Straight-Through Brazilian Disc (CSTBD) tests.

Key findings from the integrated experimental and numerical investigation include:

1. **Optimal Dosages for Mechanical Properties:** While 0.6 wt% ZnO NPs yielded the maximum compressive strength enhancement (20.6 %), an optimal dosage of 0.4 wt% proved most effective for concurrently improving tensile strength (by 40 %) and significantly boosting compressive toughness (by 86.3 %) relative to the reference UHPC. Dosages exceeding this optimum led to performance degradation, attributed to particle agglomeration.
2. **Enhanced Mixed-Mode Fracture Resistance:** The incorporation of 0.4 wt% ZnO NPs significantly increased the fracture load capacity across all crack inclination angles in CSTBD tests. The numerical model corroborated this enhancement, predicting a substantial increase in fracture toughness, particularly under shear-dominant conditions. This included shifting the critical angle (angle of minimum fracture resistance) to a lower value and markedly improving the fracture load at high angles (e.g., 56 % increase at $\beta = 90^\circ$).
3. **Significant Toughness Improvements:** The optimal ZnO NPs addition led to remarkable improvements in fracture toughness components. Notably, the Mode II fracture toughness (K_{II}) was enhanced by a factor exceeding 2.1, and the effective mixed-mode fracture toughness (K_{eff}) at the critical inclination angle (approx. 15°) increased by over 67 %.

Collectively, these findings highlight the significant potential of ZnO NPs as a strategic additive for tailoring the fracture response of UHPC. This work provides a validated framework for optimizing nano-engineered cementitious composites, paving the way for the development of materials with superior durability and resilience specifically designed for demanding structural applications subjected to complex stress states. While the current study qualitatively identified agglomeration as the mechanism of performance reduction at higher ZnO contents, direct quantitative microstructural verification was not performed. Future work should apply statistical image analysis of SEM micrographs, X-ray microtomography, or porosimetry to quantify the degree of nanoparticle clustering and its impact

Table 9
One-at-a-time sensitivity of peak load and K_{eff} to key parameters at $\beta = 45^\circ$ (values denote % change for ±10 % perturbations; signs indicate direction of change; worst of ± shown).

Parameter (symbol)	Peak load	K_{eff}
ITZ tensile strength ($f_{t,ITZ}$)	±7.8 %	±7.6 %
ITZ Mode-I fracture energy ($G_{f,I,ITZ}$)	±6.3 %	±7.1 %
ITZ shear cohesion (c_{ITZ})	±5.5 %	±5.9 %
ITZ normal stiffness (E_{ITZ})	±2.7 %	±2.9 %
CDP tensile softening slope	±5.1 %	±4.7 %
Friction/dilation angles (ITZ)	±2.2 %	±2.4 %

on pore structure. Such data will enable stronger correlations between microstructural parameters and macroscopic mechanical degradation.

The present work applied standard LEFM-based expressions for stress intensity factors to CSTBD specimens under a wide range of crack angles. While this provides valuable comparative trends, it must be recognized that LEFM is not strictly applicable under compression-shear dominated conditions (e.g., $\beta \approx 10^{\circ}$–20°). In these regimes, crack-face contact, frictional sliding, and dilatant shear fracture mechanisms are important, but not represented by the classical SIF approach. Future extensions could integrate cohesive zone models with frictional laws, contact-enriched XFEM formulations, or hybrid LEFM–cohesive models to more accurately describe mixed-mode fracture when compressive normal stresses prevail.

Engineering Recommendations. From an application perspective, the present findings suggest that UHPC incorporating ZnO nanoparticles can be optimized by adopting an addition of approximately 0.4 wt%, which maximizes tensile strength, fracture toughness, and compressive toughness while avoiding the performance degradation associated with higher dosages. For engineering practice, this dosage level can serve as a preliminary design guideline when formulating UHPC mixes for structural elements subjected to complex stress states, such as bridge decks, tunnel linings, and impact-resistant panels. In such scenarios, the enhanced mixed-mode toughness is particularly valuable in delaying crack initiation and mitigating brittle failure. Nevertheless, it is emphasized that workability and uniform dispersion of nanoparticles must be carefully controlled during mixing to ensure consistency in large-scale applications.

Future Research Directions. While this study has demonstrated the potential of ZnO NPs to improve UHPC performance under mixed-mode fracture, several aspects require further investigation:

(i) Microstructural quantification of nanoparticle agglomeration at high dosages, using statistical SEM analysis, X-ray tomography, or porosimetry;
(ii) Durability assessment of ZnO-modified UHPC under environmental exposures such as freeze–thaw, chloride ingress, carbonation, and high temperatures;
(iii) Scale-up validation in structural members to examine size effects and field constructability;
(iv) Long-term performance under sustained loading and cyclic fatigue; and
(v) Advanced modeling approaches, such as cohesive zone models with frictional contact laws, to more accurately simulate compression–shear dominated fracture regimes.Addressing these issues will facilitate the transition of ZnO-reinforced UHPC from laboratory development to reliable field deployment.

CRediT authorship contribution statement

Arzu Çağlar: Writing – review & editing, Writing – original draft, Investigation, Data curation. **Hakan Çağlar:** Writing – original draft, Software, Methodology.

Declaration of competing interest

The authors declare that they have no known competing financial interests or personal relationships that could have appeared to influence the work reported in this paper.

Data availability

Data will be made available on request.

References

[1] Sha F, Dong Y, Gu S, Fan X, Xiao W. Study on novel alkali-activated cementitious grout for scour control of offshore foundation. Geomech Energy Environ 2025;42:100663.
[2] Sharifi I, Sherzai MH, Javanmard A, Yalçındağ F, Özgür Yaman İ. Uniaxial tensile performance in the warp and weft directions of carbon textile reinforced concretes with two different matrices. Constr Build Mater 2025;476:141292.
[3] Esmaeili J, Sharifi I, Kasaei J, Nourizadeh M, Ebrahimi Emamieh A. Experimental and analytical investigation on strengthening of heat damaged concrete by textile reinforced concrete (TRC). Arch Civ Mech Engng 2019;19:1468–83.
[4] Baghal AEA, Maleki A, Sorkhabi RV. Finite element analysis of the adhesive behavior of shape memory alloy fiber and polymer concrete. J Sci Technol Compos 2021;7(4):1255–62.
[5] Baghal AEA, Maleki A, Vafaei R. On the pull-out behavior of hooked-end shape memory alloys fibers embedded in ultra-high performance concrete. Int J Eng Technol Innov 2021;11(4).
[6] Kravanja G, Mumtaz AR, Kravanja S. A comprehensive review of the advances, manufacturing, properties, innovations, environmental impact and applications of Ultra-High-Performance Concrete (UHPC). Buildings 2024;14(2):382.
[7] Yang G, Zhao H, Hu Z, Zhang W, Xiang Y, Jin M, et al. Prediction of restrained stress for UHPC: considering relationship between long-term and in-situ creep. Constr Build Mater 2025;484:141722.
[8] Wei J, Xie Z, Zhang W, Luo X, Yang Y, Chen B. Experimental study on circular steel tube-confined reinforced UHPC columns under axial loading. Engng Struct 2021;230:111599.
[9] Kim GW, Choi H-J, Piao R, Oh T, Koh K, Lim K, et al. Influence of hybrid reinforcement effects of fiber types on the mechanical properties of ultra-high-performance concrete. Constr Build Mater 2024;426:135995.
[10] Wang J, Wu Z, Han J, Wang G, Lv S. Experimental study on axial load-bearing capacity of grout-lifted compressible concrete-filled steel tube composite column. Tunn Undergr Space Technol 2025;165:106864.

[11] Pourreza T, Alijani A, Maleki VA, Kazemi A. Nonlinear vibrations of graphene nanoplates with arbitrarily orientated crack located in magnetic field using nonlocal elasticity theory. Int J Struct Integr 2025.
[12] Liu F, Tang R, Li Q, Wang H, Zou Y, Yuan X. Improved thermal performance, frost resistance, and pore structure of cement–based composites by binary modification with mPCMs/nano–SiO2. Energy 2025:137166.
[13] Su X, Ren Z, Li P. Review on physical and chemical activation strategies for ultra-high performance concrete (UHPC). Cem Concr 2024. Composites:105519.
[14] Gharebagh V, Rezazadeh G, Sharafkhani N, Shabani R. Static and dynamic response of carbon nanotube-based nano-tweezers. Int J Engng 2011;24(4):377–86.
[15] Xie J, Cao Y, Jia D, Li Y, Wang Y. Solid-state synthesis of Y-doped ZnO nanoparticles with selective-detection gas-sensing performance. Ceram Int 2016;42(1):90–6.
[16] Shutong Y, Zhongke S, Junhao W, Tiange Y, Zhenhua R, Tian L. Closed-form solution for predicting tensile strength and fracture toughness of ultra-high-performance concrete. Cem Concr Compos 2023;136:104860.
[17] Yu G, Deng Z, Wang J. Experimental study on fracture characteristics of UHPC reinforced by multiple hybrid fibers. J Beijing Univ Technol 2023;49(5):547–57.
[18] Liu R, Yang L, Wang S, Yang Y. Nitric acid-modified amorphous alloy fiber and its effects on mechanical properties of ultra-high performance concrete (UHPC). Case Stud Constr Mater 2024;21:e03956.
[19] Luo Q, Liu P, Wu M. Re-using excavated rock from underground tunneling activities to develop eco-friendly ultrahigh performance concrete. Case Stud Constr Mater 2024;20:e02867.
[20] Chen G, Zhuo K-X, Luo R-H, Lai H-M, Cai Y-J, Xie B-X, et al. Fracture behavior of environmentally friendly high-strength concrete using recycled rubber powder and steel fibers: experiment and modeling. Case Stud Constr Mater 2024;21:e03501.
[21] Tu H, Wang T, Liu C, Xu L, Chi Y. Fracture performance of ultra high performance concrete (UHPC) at different curing ages: experimental investigation and unified formulation. J Sustain Cem-Based Mater 2025:1–16.
[22] Liu Y, Xie J, Yan J-B. Flexural and fracture performance of UHPC exposed to low-temperature environment. Constr Build Mater 2023;373:130865.
[23] Zhang J, Zhan X, Yu Z, Dai Z, Du X. Study on the dynamic fracture mechanical properties of ultra high-performance concrete under the influence of steel fiber content. J Build Eng 2024;96:110540.
[24] Niu Y, Wei J, Jiao C. Crack propagation behavior of ultra-high-performance concrete (UHPC) reinforced with hybrid steel fibers under flexural loading. Constr Build Mater 2021;294:123510.
[25] Zhao S, Liu J, Liu R. Steel/plastic-steel hybrid fiber UHPC dynamic tensile performance: an experimental and numerical simulation study. J Build Eng 2024;92:109706.
[26] Chao-Shi C, Ernian P, Bernard A. Fracture mechanics analysis of cracked discs of anisotropic rock using the boundary element method. Int J Rock Mech Min Sci 1998;35(2):195–218.
[27] Xie Q, Chen D, Liu X, Zeng Y. Research on the effect of loading rate on the fracture characteristics of granite using cracked straight through Brazilian disc specimens. Theor Appl Fract Mech 2022;122:103581.
[28] Zhao Y, Deng X, Bi J, Shen M, Wang C, Zhang Y, et al. Study on the mixed fracture characteristics of concrete-rock Brazilian disks with different fracture angles. Theor Appl Fract Mech 2024;133:104614.
[29] Xu NW, Dai F, Wei MD, Xu Y, Zhao T. Numerical observation of three-dimensional wing cracking of cracked chevron notched Brazilian disc rock specimen subjected to mixed mode loading. Rock Mech Rock Engng 2015;49(1):79–96.
[30] Fowell RJ, Xu C, Dowd PA. An update on the fracture toughness testing methods related to the cracked chevron-notched Brazilian disk (CCNBD) specimen. Pageoph Top Vol 2022;65(36–59):1047–57.
[31] Hua W, Li J, Zhang W, Dong S, Tang H, Wang Y, et al. Effect of crack surface friction on stress intensity factor for double-edge cracked Brazilian disk specimens under parabolic distribution load. Theor Appl Fract Mech 2024;131:104460.
[32] Shi T, Li K-M, Wang C-Z, Jin Z, Hao X-K, Sun P, Han Y-X, Pan C-G, Fu N, Wang H-B. Fracture toughness of recycled carbon fibers reinforced cement mortar and its environmental impact assessment. Case Stud Constr Mater 2025:e04866.
[33] Long X, Mao M-H, Su T-X, Su Y-T, Tian M-K. Machine learning method to predict dynamic compressive response of concrete-like material at high strain rates. Def Technol 2023;23:100–11.
[34] Li D, Chen Q, Wang H, Shen P, Li Z, He W. Deep learning-based acoustic emission data clustering for crack evaluation of welded joints in field bridges. Autom Constr 2024;165:105540.
[35] Zheng Y, Tian Z, Yu Z, Chen J, Jiang T, Kong L, et al. A thermal history-based approach to predict mechanical properties of plasma arc additively manufactured IN625 thin-wall. J Manuf Process 2025;140:91–107.
[36] Cui X, Liu Y, Du X, Xiao H, Xu H, Du Y. Effect of fault dislocation on the deformation and damage behavior of ballastless track structures in tunnels. Transp Geotech 2025:101561.
[37] Sha F, Wang Q, Wang N, Liu F, Ni L. Performance of underwater shield synchronous double-liquid plastic grout with high W/C and volume ratio. Constr Build Mater 2025;465:140172.
[38] Wang M, Fang Z, Li X, Kang J, Wei Y, Wang S, et al. Research on the prediction method of 3D surface deformation in filling mining based on InSAR-IPIM. Energy Sci Engng 2025;13(5):2401–14.
[39] Gao D, Li Z, Ding C, Yu Z. Uniaxial tensile stress-strain constitutive relationship of 3D/4D/5D steel fiber-reinforced concrete. Constr Build Mater 2025;470:140539.
[40] Alizadeh MH, Ajri M, Maleki VA. Mechanical properties prediction of ductile iron with spherical graphite using multi-scale finite element model. Phys Scr 2023;98(12):125270.
[41] Pouraminian M, Akbari Baghal AE, Andalibi K, Khosravi F, Arab Maleki V. Enhancing the pull-out behavior of ribbed steel bars in CNT-modified UHPFRC using recycled steel fibers from waste tires: a multiscale finite element study. Sci Rep 2024;14(1):19939.
[42] Esmaeili J, Andalibi K, Gencel O, Maleki FK, Maleki VA. Pull-out and bond-slip performance of steel fibers with various ends shapes embedded in polymer-modified concrete. Constr Build Mater 2021;271:121531.
[43] Sun L, Wang X, Zhang C. Three-dimensional high fidelity mesoscale rapid modelling algorithm for concrete. Structures. Elsevier; 2024.
[44] Zhang W, Liu X, Huang Y, Tong M-N. Reliability-based analysis of the flexural strength of concrete beams reinforced with hybrid BFRP and steel rebars. Arch Civ Mech Engng 2022;22(4):171.
[45] Cuong NH, An H, Han T-V, An S, Shin J, Lee K. Structural test and FEM analysis of a thermal bridge connection employing the UHPC system for concrete cladding wall. Results Engng 2024;22:102191.
[46] Khani N, Yildiz M, Koc B. Elastic properties of coiled carbon nanotube reinforced nanocomposite: a finite element study. Mater Des 2016;109:123–32.
[47] Vahidi Pashaki P, Pouya M, Maleki VA. High-speed cryogenic machining of the carbon nanotube reinforced nanocomposites: Finite element analysis and simulation. Proc Inst Mech Engng C J Mech Engng Sci 2018;232(11):1927–36.
[48] Esmaeili J, Sharifi I, Andalibi K, Kasaei J. *Effect of different matrix* compositions and micro steel fibers on tensile behavior of textile reinforced concrete. IOP conference series: materials science and engineering. IOP Publishing; 2017.
[49] Esmaeili J, Ghaffarinia M. Multi-Scale finite element investigations into the flexural behavior of lightweight concrete beams partially reinforced with steel fiber. Comput Concr 2022;29(6):393–405.
[50] Deng Z, Chen P, Liu X, Du L, Tan J, Liang N. Study on the tensile and compressive mechanical properties of multi-scale fiber-reinforced concrete: Laboratory test and mesoscopic numerical simulation. J Build Eng 2024;86:108852.
[51] Ong CB, Ng LY, Mohammad AW. A review of ZnO nanoparticles as solar photocatalysts: Synthesis, mechanisms and applications. Renew Sustain Energy Rev 2018;81:536–51.
[52] Paillère AM. Application of admixtures in concrete. Vol. 10; 1994, CRC Press.
[53] Jorbat MH, Hosseini M, Mahdikhani M. Effect of polypropylene fibers on the mode I, mode II, and mixed-mode fracture toughness and crack propagation in fiber-reinforced concrete. Theor Appl Fract Mech 2020;109:102723.

[54] Taghibeigi H, Zeinedini A, Oleiwi AH. On the mixed mode I/II translaminar fracture of plain-weave carbon, E-glass and Kevlar reinforced laminated composites. Compos Sci Technol 2023;241:110117.
[55] Hafezolghorani M, Hejazi F, Vaghei R, Jaafar MSB, Karimzade K. Simplified damage plasticity model for concrete. Struct Engng Int 2017;27(1):68–78.
[56] Nayak CB, Taware PP, Jagadale UT, Jadhav NA, Morkhade SG. Effect of SiO2 and ZnO nano-composites on mechanical and chemical properties of modified concrete. Iran J Sci Technol Trans Civil Eng 2022;46(2):1237–47.
[57] Wei X, Xiaoqing W, Chunmei L. Effect of nano-TiO2 and polypropylene fiber on mechanical properties and durability of recycled aggregate concrete. Int J Concr Struct Mater 2024;18(1):28.
[58] Hu H, Wu F, Chen J, Guan S, Qu P, Zhang H, et al. Experimental study on cement-based materials modified by nano-zinc oxide and nano-zirconia based on response surface optimization design. Materials 2025;18(7):1515.
[59] Maleki FK, Nasution MK, Gok MS, Maleki VA. An experimental investigation on mechanical properties of Fe2O3 microparticles reinforced polypropylene. J Mater Res Technol 2022;16:229–37.